3-mm spectral line survey of two lines of sight towards two typical cloud complexes in the Galactic Centre

J. Armijos-Abendaño,[1][★] J. Martín-Pintado,[1] M. A. Requena-Torres,[2] S. Martín[3] and A. Rodríguez-Franco[4]

[1]*Centro de Astrobiología (INTA-CSIC), Ctra a Ajalvir, km 4, 28850, Torrejón de Ardoz, Madrid, Spain*
[2]*Max-Planck Institut für Radioastronomie, Auf dem Hügel 69, D-53121 Bonn, Germany*
[3]*European Southern Observatory, Alonso de Córdova 3107, Vitacura, casilla 19001, Santiago 19, Chile*
[4]*Facultad de Óptica y Optometría, Departamento de Matemática Aplicada (Biomatemática), Universidad Complutense de Madrid, Avenida de arcos de Jalón, 118, E-28037 Madrid, Spain*

ABSTRACT

We present the results of two Mopra 3-mm spectral line surveys of the lines of sight (LOS) towards the Galactic Centre (GC) molecular complexes Sgr B2 (LOS+0.693) and Sgr A (LOS−0.11). The spectra covered the frequency ranges of ∼77–93 GHz and ∼105–113 GHz. We have detected 38 molecular species and 25 isotopologues. The isotopic ratios derived from column density ratios are consistent with the canonical values, indicating that chemical isotopic fractionation and/or selective photodissociation can be considered negligible (<10 per cent) for the GC physical conditions. The derived abundances and rotational temperatures are very similar for both LOSs, indicating very similar chemical and excitation conditions for the molecular gas in the GC. The excitation conditions are also very similar to those found for the nucleus of the starburst galaxy NGC 253. We report for the first time the detection of HCO and HOC^+ emission in LOS+0.693. Our comparison of the abundance ratios between CS, HCO, HOC^+ and HCO^+ found in the two LOSs with those in typical Galactic photodissociation regions (PDRs) and starbursts galaxies does not show any clear trend to distinguish between ultraviolet- and X-ray-induced chemistries. We propose that the CS/HOC^+ ratio could be used as a tracer of the PDR components in the molecular clouds in the nuclei of galaxies.

Key words: ISM: abundances – ISM: clouds – ISM: molecules – Galaxy: centre.

1 INTRODUCTION

In this paper we study the physical conditions and chemical complexity of the quiescent molecular gas along two lines of sight (LOS), one towards the Sgr B2 complex (LOS+0.693) and the other one towards the Sgr A complex (LOS−0.11), both complexes located in the Galactic Centre (GC). Molecular cloud complexes inside the central molecular zone (Morris & Serabyn 1996) in the GC show very different characteristics than the clouds in the Galactic disk. GC clouds are characterized by high gas-kinetic temperatures of $\gtrsim$100 K (Hüttemeister et al. 1993; Rodríguez-Fernández et al. 2001) and cold dust temperatures $T_{dust} \lesssim 30$ K (Rodríguez-Fernández et al. 2004).

The Sgr B2 complex contains one of the most outstanding massive star formation sites in the Galaxy and consists of several star-forming cores embedded in a lower density envelope (Gordon et al. 1993). Sgr B2 hosts many dozens of compact and hypercom-

pact H II regions, e.g. De Pree et al. (1996) and De Pree, Goss & Gaume (1998), concentrated in two regions, Sgr B2N and Sgr B2M. LOS+0.693, which is towards the Sgr B2 molecular complex studied in this paper, is shown in Fig. 1 (upper and middle panels). It is outside the H II region L (Mehringer, Palmer & Goss 1995) and the main massive star-forming regions Sgr B2M and Sgr B2N (Martín-Pintado et al. 1990). Therefore, LOS+0.693 does not appear to be affected strongly by ultraviolet (UV) radiation, but otherwise this LOS may be subjected to significant X-ray irradiation since the Sgr B2 cloud is a well-established X-ray reflection nebula due to its strong Fe Kα line emission at 6.4 keV (Koyama et al. 1996).

The Sgr A molecular complex contains two massive molecular clouds at 20 and 50 km s^{-1}, which are believed to be interacting with the circumnuclear disk surrounding the central supermassive black hole Sgr A* and two supernova remnants, Sgr A East and G359−0.09 (Coil & Ho 2000; Herrnstein & Ho 2002; Ferrière 2012). LOS−0.11, which is towards the 20 km s^{-1} molecular cloud, is shown in Fig. 1 (bottom panels). It is located in projection 216 arcsec (∼8.6 pc) south of the black hole Sgr A*. LOS−0.11 lies near the

★E-mail: armijosaj@cab.inta-csic.es
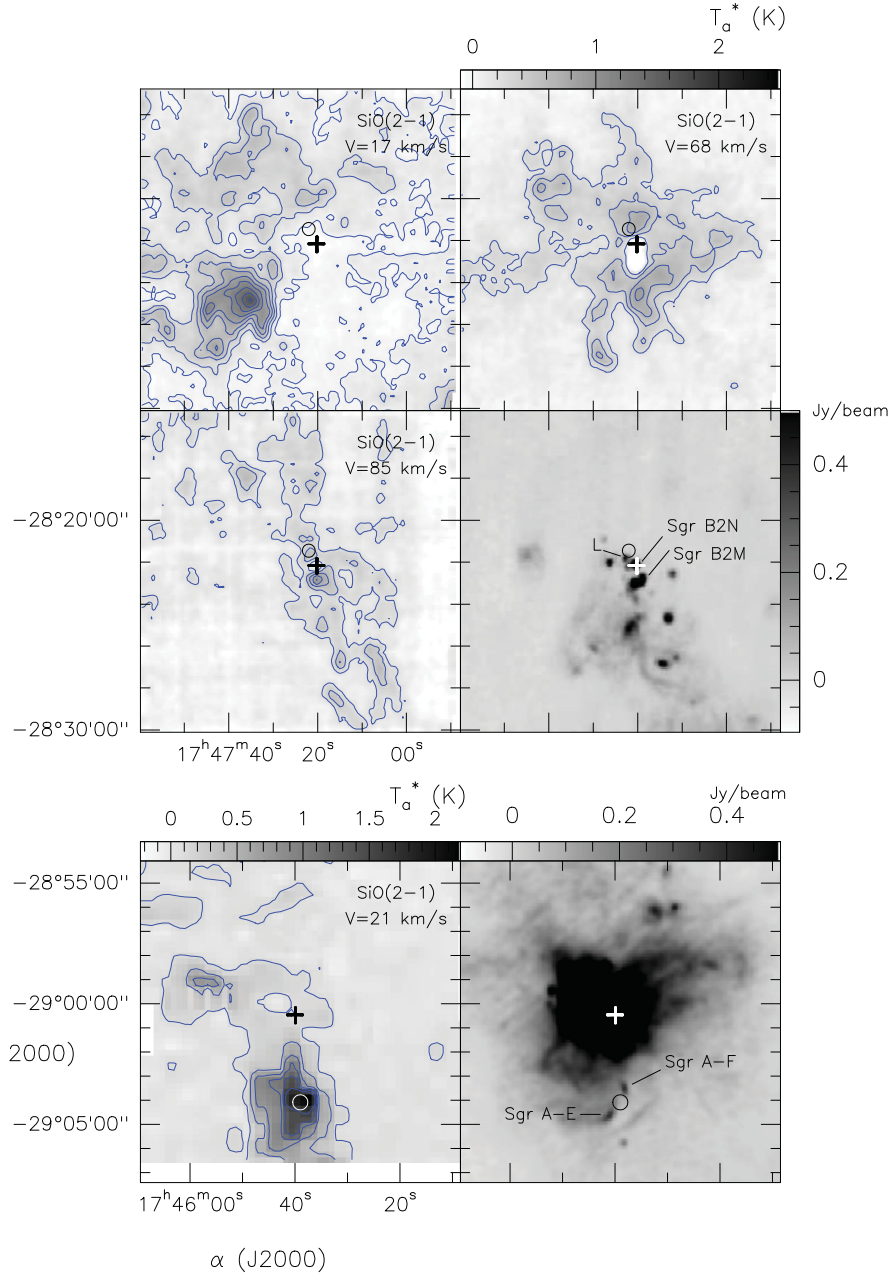
Figure 1. (Upper and middle panels) From left to right and top to bottom, SiO(2-1) large-scale emission (Martín-Pintado, private communication) maps for velocities of 17, 68 and 85 km s^{-1} and 20-cm radio continuum map (Yusef-Zadeh, Hewitt & Cotton 2004) of the Sgr B2 complex. LOS+0.693 is shown as a circle with the size of the Mopra telescope beam (38 arcsec at 90 GHz) on the SiO(2-1) and 20-cm radio continuum maps. The crosses indicate the position of the massive hot core Sgr B2N on the four maps. The position of the H II region L is indicated on the 20-cm radio continuum map. (Bottom panels) From left to right, SiO(2-1) large-scale emission (Amo-Baladrón, private communication) map for the velocity of 21 km s^{-1} and 20-cm radio continuum map (Yusef-Zadeh, Hewitt & Cotton 2004) of the Sgr A complex. LOS−0.11 is shown as a circle with the size of the Mopra telescope beam on the SiO(2-1) and 20-cm radio continuum maps. The crosses on the two maps show the position of the compact radio source Sgr A* corresponding to the central supermassive black hole. The features Sgr A-E and Sgr A-F are indicated with lines on the 20-cm radio continuum map.

elongated non-thermal features Sgr A-F and Sgr A-E (Yusef-Zadeh & Morris 1987; Lu, Wang & Lang 2003; Yusef-Zadeh et al. 2005) indicated in Fig. 1. Recent star formation (compact H II regions G−0.02-0.007) around Sgr A* is mainly concentrated towards the 50 km s^{-1} molecular cloud (Mills et at. 2011).

Unlike the star-forming regions of Sgr B2M and Sgr B2N, the selected LOSs towards the cloud positions in the Sgr B2 and Sgr A complexes studied in this paper do not show any signposts of massive star formation like H$_2$O masers, ultracompact H II regions,

hot cores or recombination line emission (Hüttemeister et al. 1993; Martín-Pintado et al. 1997).

Several unbiased spectral line surveys have been carried out towards the the Sgr B2 star-forming cores of Sgr B2N (Nummelin et al. 1998, 2000; Friedel et al. 2004; Belloche et al. 2013), Sgr B2M (Sutton et al. 1991; Belloche et al. 2013), Sgr B2S and B2OH (Friedel et al. 2004). Nummelin et al. (1998, 2000) also carried out a spectral survey towards a quiescent region in Sgr B2. They detected 26 species and showed a large difference in chemical complexity and

excitation between the quiescent and the star-forming clouds. Our line survey of two quiescent LOSs was selected from the systematic study of the HNCO/CS ratios carried out by Martín et al. (2008). In this study both locations were among the objects which had the highest ratios, indicating that the chemistry and likely the heating of both GC LOSs are mainly dominated by low-velocity shocks. This is also supported by Requena-Torres et al. (2008), who studied several GC sources, including our two LOSs, finding that the abundances of complex organic molecules like CH_2OHCHO, $(CH_3)_2O$, CH_3CHO, among others, are larger in these GC LOSs than those in hot cores of the Galactic disk, suggesting ejection of molecules from dust grains by low-velocity C-type shocks. Previous surveys of the Sgr B2 quiescent clouds by Nummelin et al. (1998, 2000) at high frequencies did not have the sensitivity to detect weak molecular lines from these species.

In this paper, we present a 3-mm spectral line survey of the quiescent molecular gas along LOS+0.693 and LOS−0.11 towards the Sgr B2 and Sgr A complexes, respectively. Both complexes, which are inside the central molecular zone, are outstanding regions affected by high-energy phenomena (Koyama et al. 1996; Terrier et al. 2010; Ponti et al. 2010) and large-scale shocks (Martín-Pintado et al. 2001). Our sensitivity allowed us to detect, for the first time, the emissions of HCO and HOC^+ molecules, which are considered to be tracers of UV radiation and X-ray chemistry in molecular clouds. In Section 2, we present our observations and data reduction. In Section 3, the details of the line identification (Section 3.1), line profiles (Section 3.2) and analysis (Section 3.3) are reported. In Section 3.4 we derive six isotopic ratios and discuss their implications. In Section 4, we discuss the molecular abundance and excitation conditions found in the GC and compare them with those in galactic nuclei (Section 4.1), and the implication of our detection of HCO and HOC^+ in the UV- and X-ray-induced chemistry in galactic nuclei (Section 4.2). Finally, the conclusions are summarized in Section 5.

2 OBSERVATIONS AND DATA REDUCTION

The observations were carried out with the 22-m Mopra radio telescope[1] in November 2007. We used the dual 3-mm Monolithic Microwave Integrated Circuit (MMIC) receiver connected to the 8-GHz spectrometer, which provided a velocity resolution of ∼0.9 km s^{-1} at 90 GHz. Spectra in two polarizations were observed simultaneously. Two frequency ranges in the 3-mm window were covered, ∼77–93 GHz and ∼105–113 GHz. The beam size of the telescope was 38 arcsec at 90 GHz and 30 arcsec at 115 GHz. We used position switching as the observing mode with the emission free reference positions selected from the CS maps obtained by Bally, Stark & Wilson (1987). The nominal positions used for the observation of LOS+0.693 and LOS−0.11 were $\alpha_{J2000} = 17^h47^m22\overset{s}{.}0$, $\delta_{J2000} = -28°21'27\overset{''}{.}0$ and $\alpha_{J2000} = 17^h45^m39\overset{s}{.}0$, $\delta_{J2000} = -29°04'05\overset{''}{.}0$, respectively. Fig. 1 shows the two observed positions superimposed on the SiO(2–1) (Martín-Pintado & Amo-Baladrón, private communication) and the 20-cm radio continuum maps (Yusef-Zadeh, Hewitt & Cotton 2004) of the Sgr B2 and Sgr A complexes. The reference positions were $\alpha_{J2000} = 17^h46^m23\overset{s}{.}0$, $\delta_{J2000} = -28°16'37\overset{''}{.}3$ and $\alpha_{J2000} = 17^h46^m00\overset{s}{.}1$, $\delta_{J2000} = -29°16'47\overset{''}{.}2$ for LOS+0.693 and LOS−0.11, respectively.

---

[1] Mopra is operated by the Australia Telescope National Facility, CSIRO and the University of New South Wales.

The raw data were reduced using the ATNF Spectral Analysis Package (ASAP) at the Mopra telescope to create the fits files for further processing with the MASSAIJ package,[2] where baseline subtraction was applied. In several regions of the spectra there were baseline ripples, which were partially corrected by editing the data in the Fourier transformed plane. The two polarizations of the spectra were averaged to improve the signal-to-noise ratio. The spectra were then smoothed to a velocity resolution of ∼3.5 km s^{-1}, appropriate for the linewidths of ∼20 km s^{-1} observed towards molecular clouds in the GC. Our line intensities in T_A^* units are affected by 20–30 per cent uncertainties in the calibration procedure based on a noise diode and an ambient temperature load.

3 RESULTS

3.1 Line identification

The 3-mm spectra observed towards both LOSs are shown in Fig. 2, and identified molecules and unidentified lines are indicated. Representative samples of line profiles for several molecular transitions and their isotopologues for LOS+0.693 and LOS−0.11 are shown in Figs 3 and 4, respectively. The molecular identification and analysis were carried out using the frequencies and the spectroscopic information from the Jet Propulsion Laboratory (JPL) (Pickett et al. 1998) and Cologne Database for Molecular Spectroscopy (CDMS) (Müller et al. 2001, 2005) catalogues contained in the MASSAIJ package. For LOS+0.693, we found 38 molecular species and 25 isotopologues, as well as 18 unidentified lines. In contrast, for LOS−0.11, we found only 34 molecular species and 18 isotopologues, as well as eight unidentified lines.

In our survey, we detected, for the first time, HCO and HOC^+ emissions towards the quiescent gas of LOS+0.693 in the GC outside the hot cores of Sgr B2N and Sgr B2M. We detected four HCO hyperfine lines ($F = 2–1$, 1–0, 1–1 and 0–1) and one HOC^+(1–0) line towards LOS+0.693 (see Figs 2 and 3). HCO, HOC^+, HC_2NC and $HCOCH_2OH$ were not detected towards LOS−0.11 (see Figs 2 and 4). It has been proposed that HCO and HOC^+ molecules are tracers of photodissociation regions (PDRs) (Apponi, Pesch & Ziurys 1999; Goicoechea et al. 2009; Martín, Martín-Pintado & Viti 2009b) and X-ray dominated regions (XDRs) (Usero et al. 2004). Tables 1 and 2 show the line parameters derived by Gaussian fitting to almost all observed molecular lines for both LOSs. The tables also include, for both LOSs, upper limits to the emission of several molecular species, like HOC^+ and HCO, which are relevant for the discussion. These upper limits (4 for LOS+0.693 and 16 for LOS−0.11) correspond to 3σ of the peak and velocity-integrated intensities (see Tables 1 and 2).

3.2 Line profiles

Most line profiles from each cloud trace just their kinematic structure, i.e. three velocity components (∼17, 68 and 85 km s^{-1}) in LOS+0.693 and one velocity component (∼20 km s^{-1}) in LOS−0.11. Additional double-peaked line profiles of certain strong molecular species like HCO^+, HNC and HCN are likely a result of optical depth effects, as this double-peaked structure is not present in the line profiles of their optically thin isotopologues. In this paper,

---

[2] This package has been developed at the Centro de Astrobiología. More information about this package can be found at http://cab.inta-csic.es/madcuba/Portada.html.

Figure 2. 3-mm spectra of LOS+0.693 (left panels) and LOS−0.11 (right panels). Each panel shows a spectrum with a ∼2 GHz coverage. Detected transitions of known molecules are indicated, while unidentified lines are labelled U. Some regions of the spectra affected by ripples are indicated with the letter R.

we will concentrate on emissions from the 68 and 85 km s⁻¹ clouds along LOS+0.693 and the ∼20 km s⁻¹ cloud along LOS−0.11.

To compare molecular abundances derived from optically thick lines (e.g. CN, HNC, HCN, HCO⁺ and CH₃OH) with those showing simpler profiles we have calculated, in Tables 1 and 2, their velocity-

integrated intensities over the selected velocity ranges given in column 4 of these tables. For LOS+0.693 we have considered two velocity ranges of 40–80 km s⁻¹ and 80–110 km s⁻¹ corresponding to the emission of the ∼68 and ∼85 km s⁻¹ clouds, respectively. For LOS−0.11, we have derived velocity-integrated intensities only for

Figure 2 – *continued*

HCO$^+$(1–0) and HCN(1–0) lines and their corresponding isotopologues.

Figs 3 and 4 present the line profiles of all detected methanol transitions for LOS+0.693 and LOS−0.11, respectively. Interestingly the CH$_3$OH($3_{1,3}$–$4_{0,4}$) line is the only methanol line observed in ab-

sorption in our survey, while the CH$_3$OH($0_{0,0}$–$1_{-1,1}$) line appears to be optically thick in both LOSs. Furthermore, the CH$_3$OH($5_{-1,5}$–$4_{0,4}$) line at 84.5 GHz is intense and it has been reported to be masing in some sources (Zuckerman et al. 1972; Batrla & Menten 1988).

(a)

(b)

Figure 3. Sample of molecular lines and their isotopologues observed towards LOS+0.693. We used the column densities derived from these transitions and others to estimate the carbon, nitrogen, oxygen, sulfur and silicon isotopic ratios. The vertical dashed lines show the local standard of rest (LSR) velocities of 17, 68 and 85 km s^{-1}.

3.3 Analysis

Assuming optically thin emission and excitation in local thermodynamic equilibrium (LTE), the relation between the LTE total molecular column density N and the measured integrated line intensity, $W = \int T_A^* d\upsilon$ in K km s^{-1}, of a transition is given by:

$$\frac{N_u}{g_u} = \frac{N}{Q_{rot}} e^{-E_u/kT_{rot}} = \frac{1.67 \times 10^{14} W}{\nu \mu^2 S} \qquad (1)$$

where N_u is the molecular column density in the upper energy level, g_u and E_u/k are the degeneracy and the energy (in kelvin) of the upper level of the transition with a frequency ν in gigahertz, a dipole moment μ in debye and a line strength S. T_{rot} is the LTE rotational temperature in kelvin and Q_{rot} is the rotational partition function. Taking the natural logarithm in (1), we obtain the main equation for the rotational diagrams (RDs):

$$\ln \frac{1.67 \times 10^{14} W}{\nu \mu^2 S} = \ln \frac{N}{Q_{rot}} - \frac{E_u}{kT_{rot}}. \qquad (2)$$

By observing more than one transition from the same molecule, we can estimate the excitation temperature of the rotational levels, T_{rot}, and the LTE total column densities (by using Q_{rot} for T_{rot}) from a linear regression fit to equation (2). Since the typical uncertainties of assuming the Rayleigh–Jeans approximation are less than the calibration uncertainties, they are ignored.

3.3.1 Rotational temperatures and molecular column densities

We used the MASSAIJ package with spectroscopic information (A_{ul}, g_u, E_u, $\mu^2 S$, Q_{rot}, etc.) from the JPL and CDMS catalogues to generate the RDs for all molecules with more than one observed transition. Fig. 5 shows RDs (for both GC sources) for selected molecules, and the derived T_{rot} from RDs are listed in Table 3. All RDs are fitted with a single T_{rot}. The uncertainties in the T_{rot} are derived from the 1σ uncertainties in the integrated line intensities and also take into account the uncertainty due to the linear regression

(a)

(b)
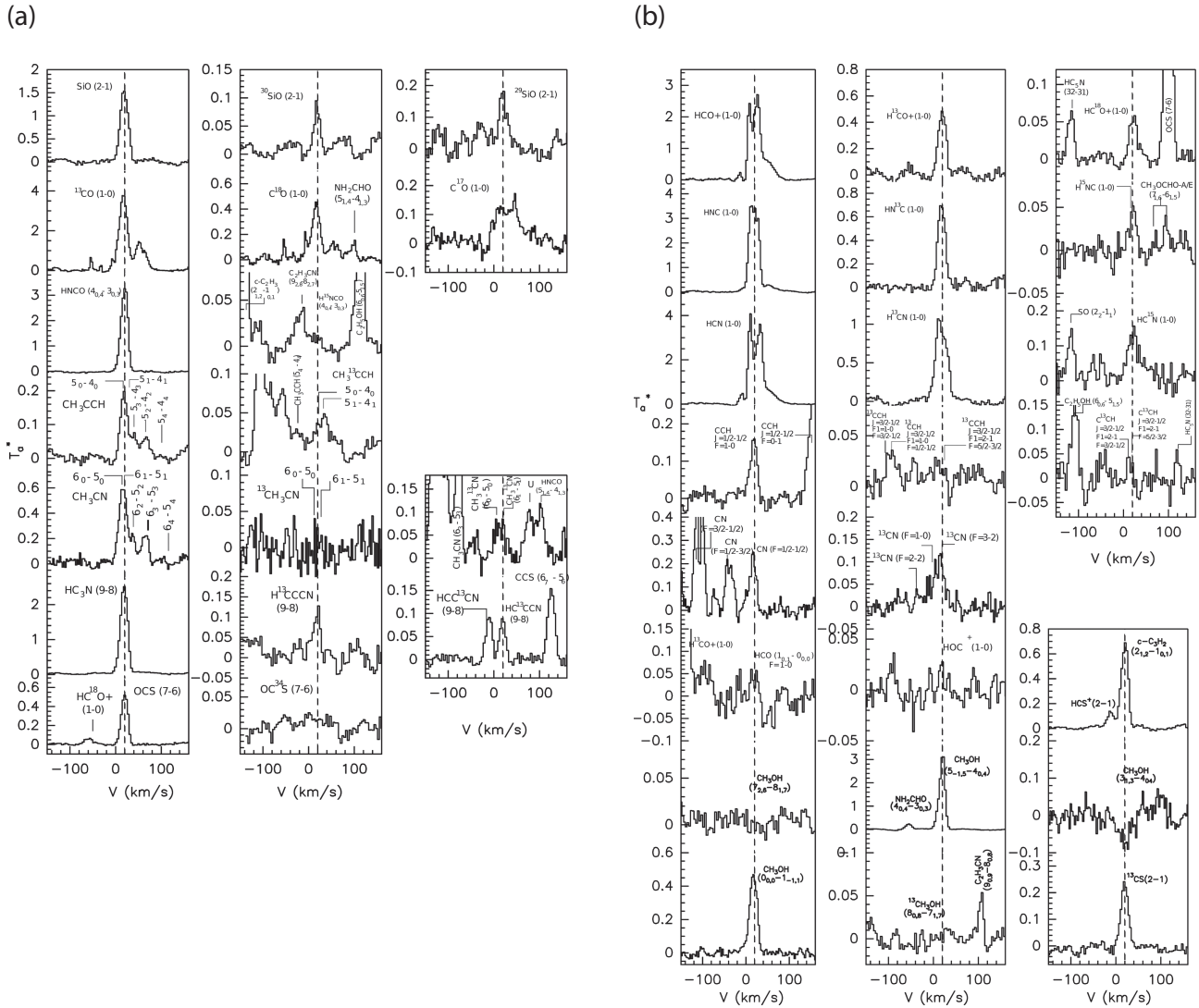
Figure 4. Sample of molecular lines and their isotopologues observed towards LOS−0.11. We used the column densities derived from these transitions and others to estimate the carbon, nitrogen, oxygen, sulfur and silicon isotopic ratios. The vertical dashed line shows the LSR velocity of 20 km s^{-1}.

Table 1. Line parameters for LOS+0.693. The full table will be available in the online edition of the journal.

Molecule	Frequency (MHz)	Transition	Area (σ) (K km s^{-1})	V_{LSR} (σ) (km s^{-1})	$\Delta_{v_{1/2}}$ (σ) (km s^{-1})	T_a^* (σ) (mK)	Notes
C_2H_3CN	77 633.8	$8_{1,7}-7_{1,6}$	2.6 (0.5)	63.9 (1.4)	19.6 (3.2)	125.8 (15.6)	
Unidentified	77 935.5	–	2.9 (1.1)	65.0 (5.0)	25.0 (5.0)	88.1 (18.2)	
C_2H_5CN	78 183.6	$9_{1,9}-8_{1,8}$	3.6 (0.6)	64.2 (1.5)	30.5 (3.5)	111.0 (11.9)	
CH_3OCHO^b	78 481.3	$7_{1,7}-6_{1,6}$ A+E	1.7 (0.4)	71.7 (1.4)	24.8 (2.7)	129.5 (7.6)	bl
CH_3CHO	79 099.3	$4_{1,3}-3_{1,2}$ E	5.6 (0.4)	70.5 (0.4)	20.7 (1.0)	0.3 (11.6)	
CH_3CHO	79 150.2	$4_{1,3}-3_{1,2}$ A	10.0 (0.6)	70.9 (0.4)	22.5 (1.0)	418.0^a (16.1)	
$H^{13}CCCN$	79 350.4	$9_K-8_K, K = 8-7, 9-8, 10-9$	4.9 (0.3)	70.5 (0.5)	22.8 (1.3)	202.6 (8.8)	hf
NH_2CN	79 449.7	$4_{1,4}-3_{1,3}$	10.9 (0.5)	68.4 (0.3)	19.2 (0.7)	534.9 (14.2)	
C_2H_5CN	79 677.5	$9_{0,9}-8_{0,8}$	2.6 (0.5)	64.3 (1.9)	29.2 (4.5)	83.8 (11.5)	
H_2C_2N	79 759.4	$4_{1,4}-3_{1,3}, J = 9/2-7/2$	2.1 (0.5)	65.9^a (1.7)	19.1^a (3.9)	103.7 (7.3)	hf^a

Notes. bl: Blended line. hf: Hyperfine structure (frequency refers to the main component of the group). hf^a: Hyperfine component (it is possible to resolve this hyperfine component since its frequency is sufficiently far from the frequencies of the other hyperfine components). ^{a} Parameter fixed in the Gaussian fit. ^{b} Frequency refers to species A.

Table 2. Line parameters for LOS−0.11. The full table will be available in the online edition of the journal.

Molecule	Frequency (MHz)	Transition	Area (σ) (K km s^{-1})	V_{LSR} (σ) (km s^{-1})	$\Delta_{v_{1/2}}$ (σ) (km s^{-1})	T_a^* (σ) (mK)	Notes
C_2H_3CN	77 633.8	$8_{1,7}-7_{1,6}$	1.8 (0.4)	21.9 (1.2)	19.6 (2.9)	88.0 (12.0)	
CH_3CHO	79 099.3	$4_{1,3}-3_{1,2}$ E	4.8 (0.5)	20.3 (0.7)	20.2 (1.6)	222.1 (15.6)	
CH_3CHO	79 150.2	$4_{1,3}-3_{1,2}$ A	4.5 (0.8)	17.5 (1.2)	19.2 (2.7)	220.0^a (23.9)	
$H^{13}CCCN$	79 350.4	9_K-8_K, $K = 8-7$, 9–8, 10–9	2.7 (0.5)	16.7 (1.1)	19.2 (2.8)	131.0^a (11.7)	hf
NH_2CN	79 449.7	$4_{1,4}-3_{1,3}$	5.9 (0.4)	20.1 (0.4)	19.2 (1.0)	290.0^a (11.7)	
C_2H_5CN	79 677.5	$9_{0,9}-8_{0,8}$	1.8 (0.3)	16.2 (1.2)	19.1 (2.9)	87.0^a (9.4)	
HC_5N	79 876.9	30–29	2.4 (0.3)	18.2 (0.8)	19.6 (1.8)	115.8 (9.4)	
NH_2CN	79 963.2	$4_{2,3}-3_{2,2}$	1.3 (0.3)	17.6 (1.5)	19.0 (3.6)	65.0^a (9.3)	m
NH_2CN	79 979.5	$4_{0,4}-3_{0,3}$	2.5 (0.4)	21.2 (1.0)	19.0 (2.4)	124.0^a (13.1)	
CH_2CO	80 076.7	$4_{1,4}-3_{1,3}$	2.2 (0.2)	20.7 (0.5)	17.2 (1.1)	119.6 (6.2)	

Notes. bl: Blended line. hf: Hyperfine structure (frequency refers to the main component of the group). hf^a: Hyperfine component (it is possible to resolve this hyperfine component since its frequency is sufficiently far from the frequencies of the other hyperfine components).
^{a}Parameter fixed in the Gaussian fit.

fit in the RDs. In our survey, the derived T_{rot} ranges from 5 to 73 K (see Table 3); however, most of the derived T_{rot} are rather low compared with the estimated mean kinetic temperature of $\approx$100 K found in the GC (Güsten et al. 1985; Hüttemeister et al. 1993), indicating subthermal excitation due to relatively low H_2 densities (see Section 3.3.4).

Molecular lines contaminated by the emission from unidentified molecular species (see notes in Tables 1 and 2) are not included in the RDs. When required, we have also properly taken into account the hyperfine structure (see notes in Tables 1 and 2) to estimate the total column densities given in Table 3. We have used equation (1) to estimate the total column densities for molecules with only one detected transition by assuming $T_{rot} = 10$ K, the average value of the low T_{rot} derived from other molecules (see Table 3). We have also used $T_{rot} = 10$ K to derive the column densities of molecular species with several observed transitions but with insufficient dynamical range in E_u ($\lesssim$2 K) to derive a reliable T_{rot}.

To avoid the uncertainties introduced by optical depth effects in the estimated column densities of molecules like HCN, HNC and HCO$^+$, in Table 3, when possible, we have derived them from the optically thin lines (see note b in Table 3) of their rarer isotopologues, assuming the typical GC isotopic ratios (Wilson & Rood 1994, hereafter W&R94). The LTE approximation used in our analysis provides beam-averaged abundances that are relatively similar to those obtained by using non-LTE statistical equilibrium methods. The difference in the estimated HC$_3$N column densities using the LTE and non-LTE analysis is less than a factor of $\sim$2 for both GC sources (see Section 3.3.4).

To derive the CH$_3$OH column density for LOS+0.693 we have used the $7_{2,6}-8_{1,7}$ transition and $T_{rot} = 14$ K derived by Requena-Torres et al. (2008). This transition is selected since it shows thermal emission, is likely optically thin, and is observed in emission towards LOS+0.693 (see Section 3.2). For LOS−0.11, this methanol transition is not detected, so we have derived only an upper limit for the methanol column density by assuming $T_{rot} = 13$ K derived by Requena-Torres et al. (2008).

3.3.2 H_2 column densities and molecular abundances

To estimate the molecular fractional abundances relative to H_2, we need to estimate the H_2 column density (N_{H_2}) towards both LOSs. We have used the C^{18}O lines to estimate the H_2 column densities by assuming a ^{16}O/^{18}O isotopic ratio of 250 (W&R94) and a relative abundance of CO to H_2 of 10^{-4} (Frerking, Langer & Wilson 1982).

We found $N_{H_2} = 5.9$ (0.2) $\times$ 10^{22} and 2.4 (0.2) $\times$ 10^{22} cm^{-2} for LOS+0.693 and LOS−0.11, respectively. The estimated relative abundances obtained by dividing the molecular column densities by their respective N_{H_2} are shown in Table 3 for the molecules and velocity components identified in our spectral line survey. Fig. 6 summarizes the derived fractional abundances from Table 3 for all species except for ^{13}C^{15}N (its 1–0 transition is contaminated by emission from an unknown molecular species), O^{13}C^{34}S (there is no lower limit for LOS−0.11), and HCO$^+$, HCN, HNC and their ^{13}C isotopologues, whose abundances are obtained from their less abundant isotopologues.

It is remarkable, that two LOSs separated by more than $\sim$120 pc in the GC show very similar abundances, within a factor of 2, of $\sim$80 per cent of the detected molecular species, including the most complex organic molecules like C$_2$H$_5$OH, C$_2$H$_5$CN and (CH$_3$)$_2$O (see Fig. 6). This finding will be discussed in detail in Section 4.1.1.

3.3.3 Kinetic temperatures

Symmetric rotors are usually used to estimate the kinetic temperature, T_{kin}, of molecular clouds because the radiative transitions between levels of ladders with $\Delta K \neq 0$ are forbidden (Turner 1991), and their excitation is dominated by collisions with H_2. In our survey, we detected transitions from CH$_3$CN, ^{13}CH$_3$CN, CH$_3$^{13}CN, CH$_3$CCH and CH$_3$^{13}CCH. We derived T_{rot} for both LOSs from the RDs of the 6_K-5_K ($K = 0, 1, 2, 3$ and 4) transitions of CH$_3$CN and the 6_K-5_K ($K = 0, 1, 2$ and 3) transitions of CH$_3$CCH. In addition, for LOS+0.693 we have also used the 6_K-5_K ($K = 0, 1$ and 3) transitions of ^{13}CH$_3$CN (the $K = 2$ line is not used because it is blended with the $K = 0$ and 1 lines).

As expected, the symmetric rotors CH$_3$CN, CH$_3$CCH and ^{13}CH$_3$CN show the highest $T_{rot} \approx 55–73$ K for both GC sources (see Table 3), indicating that T_{kin} must be larger than 73 K. For $T_{kin} = 100$ K, statistical equilibrium calculations reveal that T_{rot} derived from CH$_3$CN transitions with $\Delta K \neq 0$ ($K < 4$) approach T_{kin} only at H_2 densities of $\sim$10^6 cm^{-3}. For H_2 densities of $\lesssim$10^5 cm^{-3} and $T_{kin} = 100$ K, these CH$_3$CN transitions show $T_{rot} \lesssim 70$ K (Churchwell, Walmsley & Wood 1992). Our results are consistent with the mean $T_{kin} \approx 100$ K derived by Güsten et al. (1985), Hüttemeister et al. (1993) and Rodríguez-Fernández et al. (2001) towards molecular clouds distributed over the central 500 pc of the GC. Thus, for the low H_2 densities ($\sim$10^4 cm^{-3}, see Section 3.3.4) found in both GC sources, in the following discussions we will consider $T_{kin} \approx 100$ K.
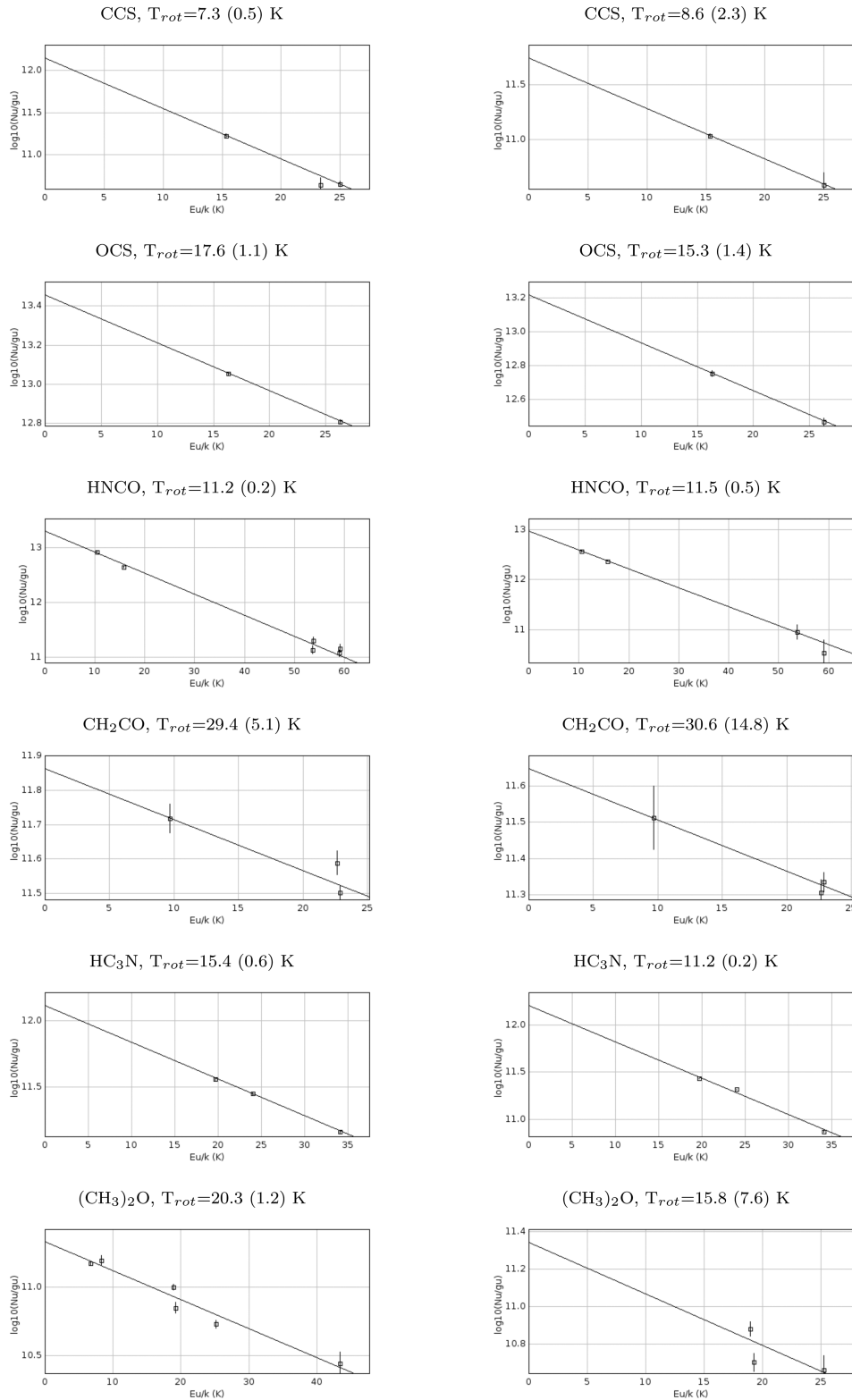
Figure 5. Rotational diagrams of some molecules for LOS+0.693 (left panels) and LOS−0.11 (right panels).

3.3.4 H_2 densities

We have used the non-LTE excitation and radiative transfer code RADEX with the large velocity gradient approximation (van der Tak et al. 2007) to estimate the H_2 densities using three HC_3N lines (see Tables 1 and 2). For $T_{kin} = 100$ K, a linewidth of 21 km s^{-1},

a background temperature of 2.73 K and a beam-filling factor of 1 (since the cloud size is much larger than the telescope beam size, see Fig. 1), we have estimated H_2 densities of $\sim$2.3 (0.3) $\times$ 10^4 cm^{-3} for both GC sources.

The HC_3N column densities and H_2 densities were considered free parameters for the modelling. Our non-LTE analysis provided

NH$_2$CN, T$_{rot}$=47.6 (3.1) K

NH$_2$CN, T$_{rot}$=53.6 (10.3) K

CH$_3$CN, T$_{rot}$=65.2 (6.5) K

CH$_3$CN, T$_{rot}$=63.5 (8.7) K

CH$_3$CCH, T$_{rot}$=61.1 (10.9) K

CH$_3$CCH, T$_{rot}$=54.8 (5.5) K

HC$_5$N, T$_{rot}$=32.1 (4.7) K

HC$_5$N, T$_{rot}$=44.5 (19.1) K

CH$_3$CHO-A, T$_{rot}$=5.4 (0.4) K

CH$_3$CHO-A, T$_{rot}$=4.5 (1.0) K

HOCO$^+$, T$_{rot}$=7.5 (0.4) K

HOCO$^+$, T$_{rot}$=6.5 (0.8) K
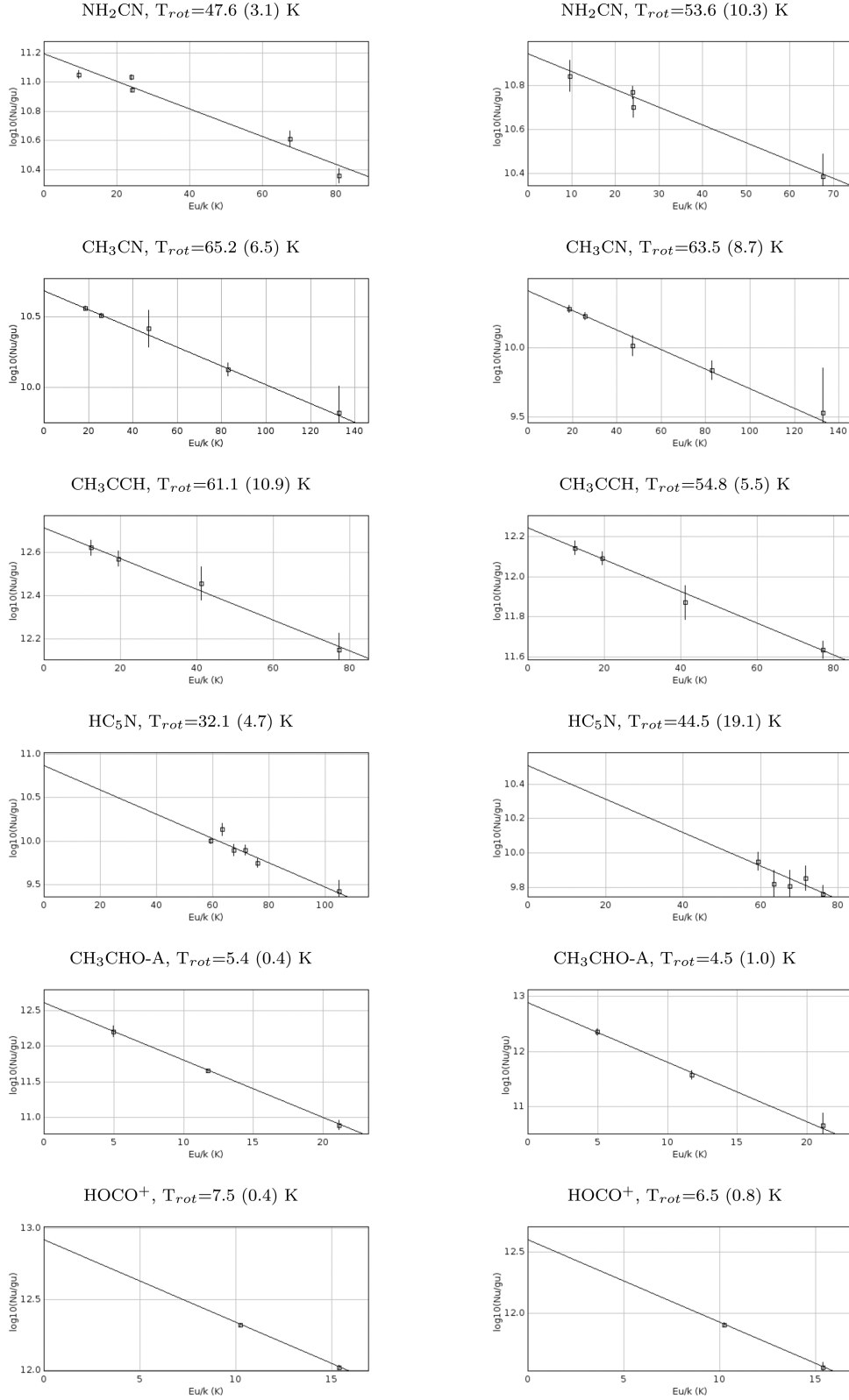
Figure 5 – *continued*

estimates of the HC$_3$N column densities of 6.0×10^{14} cm^{-2} for LOS+0.693 and 4.9×10^{14} cm^{-2} for LOS−0.11, in good agreement within a factor of 2 with the LTE calculations of the HC$_3$N column densities (see Table 3). Our estimated line optical depths are ∼0.5 for the three HC$_3$N lines. The predicted excitation temperatures of ∼14 K are also consistent with the LTE analysis and our assumption of subthermal excitation. Changes in the T_{kin} to lower values of ∼50 K, will increase the H$_2$ densities by only a factor

Table 3. T_{rot}, column densities and abundances for both LOSs.

Molecule	LOS+0.693				LOS−0.11			
	V_{LSR} (σ) (km s^{-1})	T_{rot}^a (σ) (K)	N (σ) ($\times 10^{13}$ cm^{-2})	N/N_{H_2} (σ) ($\times 10^{-9}$)	V_{LSR} (σ) (km s^{-1})	T_{rot}^a (σ) (K)	N (σ) ($\times 10^{13}$ cm^{-2})	N/N_{H_2} (σ) ($\times 10^{-9}$)
^{13}CO	–	–	28 100.0 (644.0)^b	4810.0 (112.0)	–	–	11 500.0 (953.0)^b	4790.0 (566.0)
	–	–	–	–	–	–	3010.0 (931.0)^b	1260.0 (404.0)
C^{18}O	66.8 (0.3)	–	2344.2 (91.2)^c	400.7 (22.0)	15.1 (0.6)	–	955.0 (79.4)^c	400.0 (47.0)
	–	–	–	–	55.2 (2.1)	–	251.2 (77.6)^c	105.2 (33.6)
C^{17}O	65.7 (0.7)	–	489.8 (45.7)^c	83.6 (8.5)	15.2 (3.7)	–	371.5 (102.3)^c	155.6 (44.7)
	–	–	–	–	42.9 (1.4)	–	281.8 (44.7)^c	118.1 (21.1)
CN	70.5 (0.5)	–	169.8 (17.4)^d	29.0 (3.2)	13.9 (0.6)	–	173.8 (19.5)^d	72.5 (10.1)
^{13}CN	71.3 (1.0)	–	7.4 (1.3)^d	1.1 (0.2)	21.0 (4.0)	–	7.9 (2.0)^d	3.3 (0.8)
^{13}C^{15}N^e	67.9 (1.0)	–	67.6 (5.6)^c	11.5 (1.1)	–	–	–	–
^{13}CS	[45,80]^g	–	2.3 (0.2)^c	0.4 (0.04)	18.7 (0.2)	–	2.8 (0.1)^c	1.2 (0.1)
SiO	–	–	9.0 (1.8)^b	1.4 (0.2)	18.2 (0.2)	–	7.2 (0.2)^c	3.0 (0.3)
^{29}SiO	65.6 (0.6)	–	0.5 (0.1)^c	0.09 (0.009)	21.8 (1.0)	–	0.9 (0.1)^c	0.4 (0.1)
^{30}SiO	71.8 (0.6)	–	0.5 (0.1)^c	0.08 (0.009)	19.7 (0.5)	–	0.4 (0.03)^c	0.2 (0.02)
SiS	69.5 (3.7)	–	4.5 (1.2)^c	0.8 (0.2)	21.2 (1.1)	–	1.7 (0.4)^c	0.7 (0.2)
SO	$\sim$68^f	8.1 (2.4)	61.0 (51.3)	10.4 (8.8)	$\sim$21^f	14.2 (8)	18.6 (3.7)	7.8 (2.0)
CCH	65.4 (0.4)	–	316.2 (18.6)^d	54.1 (3.8)	19.8 (0.6)	–	251.2 (24)^d	105.0 (13.3)
^{13}CCH	67.6 (2.4)	–	16.6 (3.5)^d	2.8 (0.6)	27.9 (2.3)	–	11.1 (3.0)^c	4.8 (1.3)
C^{13}CH	60.6 (1.5)	–	14.8 (2.6)^c	2.5 (0.5)	–	–	$\lesssim$8.7	$\lesssim$3.6
CCS	$\sim$67^f	7.3 (0.5)	5.6 (1.1)	1.0 (0.2)	$\sim$21^f	8.6 (2.3)	3.6 (2.3)	1.5 (1.0)
HCN	–	–	$\gtrsim$240^b	$\gtrsim$36	–	–	$\gtrsim$480^b	$\gtrsim$180
	–	–	$\gtrsim$120^b	$\gtrsim$12	–	–	–	–
H^{13}CN	–	–	$\gtrsim$11^b	$\gtrsim$2	–	–	$\gtrsim$23^b	$\gtrsim$9
	–	–	$\gtrsim$6^b	$\gtrsim$1	–	–	–	–
HC^{15}N	[40, 80]^g	–	0.4 (0.04)^c	0.06 (0.01)	[−0.8, 47.2]^g	–	0.8 (0.1)^c	0.3 (0.04)
	[80, 110]^g	–	0.2 (0.02)^c	0.02 (0.01)	–	–	–	–
HCO	68.5 (1.3)	–	6.9 (1.4)^d	1.2 (0.3)	–	–	$\lesssim$3.3	$\lesssim$1.4
HCS$^+$	70.4 (0.7)	–	2.9 (0.3)^c	0.5 (0.1)	21.8 (1.7)	–	1.4 (0.4)^c	0.6 (0.2)
HNC	–	–	$\gtrsim$240^b	$\gtrsim$42	–	–	$\gtrsim$180^b	$\gtrsim$60
HN^{13}C	–	–	$\gtrsim$11^b	$\gtrsim$2	–	–	$\gtrsim$9^b	$\gtrsim$3
H^{15}NC	[40, 80]^g	–	0.4 (0.05)^c	0.07 (0.01)	21.5 (1.3)	–	0.3 (0.1)^c	0.1 (0.01)
HNO	67.5 (0.8)	–	3.2 (0.4)^c	0.6 (0.08)	17.2 (1.2)	–	2.5 (0.5)^c	1.0 (0.2)
HOC$^+$	68.0 (0.8)	–	0.1 (0.01)^c	0.02 (0.003)	–	–	$\lesssim$0.03	$\lesssim$0.01
HCO$^+$, $v = 0,1,2$	–	–	57.0 (1.3)^b	9.6 (2.2)	–	–	36.0 (0.8)^b	15.5 (3.0)
H^{13}CO$^+$	–	–	2.7 (0.1)^b	0.5 (0.1)	–	–	1.7 (0.04)^b	0.7 (0.1)
HC^{18}O$^+$	74.5 (2.8)	–	0.2 (0.1)^c	0.04 (0.01)	23.4 (1.2)	–	0.2 (0.03)^c	0.06 (0.01)
OCS	$\sim$65^f	17.6 (1.1)	186.2 (4.6)	31.8 (1.5)	$\sim$19^f	15.3 (1.4)	87.1 (14.1)	36.4 (6.5)
OC^{34}S	$\sim$66^f	12.1 (2.9)	21.4 (3.1)	3.7 (0.6)	–	–	$\lesssim$4.0	$\lesssim$1.7
O^{13}CS	$\sim$66^f	11.3 (4.7)	7.8 (1.2)	1.3 (0.2)	–	–	$\lesssim$3.5	$\lesssim$1.5
O^{13}C^{34}S	–	–	$\lesssim$3.0	$\lesssim$0.5	–	–	–	–
SO$_2$	65.0 (0.4)	–	83.2 (3.4)^c	14.2 (1.0)	18.6 (1.0)	–	20.4 (3.7)^c	8.6 (1.7)
HNCO	$\sim$66^f	11.2 (0.2)	144.5 (5.6)	24.7 (1.4)	$\sim$18^f	11.5 (0.5)	67.6 (4.5)	28.3 (3.0)
H^{15}NCO	–	–	$\lesssim$0.4	$\lesssim$0.1	–	–	$\lesssim$0.3	$\lesssim$0.1
HNC^{18}O	–	–	$\lesssim$1.1	$\lesssim$0.2	–	–	$\lesssim$0.9	$\lesssim$0.4
HNCS, a-type	$\sim$66^f	15.2 (5.6)	3.1 (2.2)	0.5 (0.4)	21.2 (2.0)	–	2.0 (0.6)^c	0.8 (0.3)
HOCO$^+$	$\sim$66^f	7.5 (0.4)	12.0 (1.4)	2.1 (0.3)	$\sim$20^f	6.5 (0.8)	4.8 (1.2)	2.0 (0.6)
CH$_2$CO	$\sim$66^f	29.2 (6.8)	22.9 (6.8)	3.9 (1.2)	$\sim$19^f	30.6 (14.8)	14.8 (12.3)	6.2 (5.2)
CH$_2$NH	71.5 (1.0)	–	29.5 (4.8)^c	5.0 (0.8)	17.8 (2.6)	–	24.0 (7.8)^c	10.1 (3.4)
HC$_3$N	$\sim$70^f	15.4 (0.6)	54.9 (3.3)^b	9.4 (1.0)	$\sim$18^f	11.2 (0.2)	26.8 (0.6)	11.2 (1.0)
H^{13}CCCN	$\sim$70^f	14.4 (1.6)	2.6 (0.2)	0.5 (0.03)	$\sim$18^f	9.0 (3.0)	1.9 (0.3)	0.8 (0.2)
HC^{13}CCN	$\sim$66^f	12.0 (1.9)	2.0 (0.2)	0.4 (0.04)	$\sim$20^f	19.5 (6.1)	1.3 (0.4)	0.5 (0.2)
HCC^{13}CN	$\sim$68^f	9.4 (1.2)	2.7 (0.5)	0.5 (0.10)	$\sim$19^f	11.5 (2.2)	1.4 (0.3)	0.6 (0.1)
HCCNC	70.1 (3.1)	–	0.7 (0.3)^c	0.1 (0.05)	–	–	$\lesssim$0.9	$\lesssim$0.4
HCOOH	$\sim$67^f	18.9 (4.8)	14.4 (6.2)	2.5 (1.1)	18.6 (0.9)	–	15.9 (4.2)^d	6.6 (1.8)
H$_2$C$_2$N	70.4 (0.7)	–	11.0 (1.4)^d	1.9 (0.3)	17.6 (1.2)	–	4.8 (1.2)^d	2.0 (0.5)
NH$_2$CN	$\sim$67^f	47.6 (3.1)	11.9 (1.5)	2.0 (0.3)	$\sim$20^f	53.6 (10.3)	8.3 (3.0)	3.5 (1.3)
c-C$_3$H$_2$	$\sim$69^f	13.1 (1.9)	9.4 (2.5)	1.6 (0.4)	$\sim$20^f	6.6 (0.4)	6.0 (0.7)	2.5 (0.4)
CH$_3$CN, $v8 = 0,1$	69.7 (0.8)	65.2 (6.5)	28.0 (3.0)^b	4.8 (0.6)	$\sim$20^f	63.5 (8.7)	7.4 (1.6)	3.1 (0.7)

Table 3 – *continued*

Molecule	LOS+0.693				LOS−0.11			
	$V_{\rm LSR}$ (σ) (km s^{-1})	$T_{\rm rot}{}^a$ (σ) (K)	N (σ) ($\times 10^{13}$ cm^{-2})	$N/N_{\rm H_2}$ (σ) ($\times 10^{-9}$)	$V_{\rm LSR}$ (σ) (km s^{-1})	$T_{\rm rot}{}^a$ (σ) (K)	N (σ) ($\times 10^{13}$ cm^{-2})	$N/N_{\rm H_2}$ (σ) ($\times 10^{-9}$)
^{13}CH$_3$CN	$\sim$74^f	73.3 (32.2)	1.1 (0.7)	0.2 (0.1)	–	63.5	≲1.5	≲0.6
CH$_3^{13}$CN	69.7 (0.8)	73.3	1.4 (0.2)^d	0.2 (0.03)	–	63.5	≲1.9	≲0.8
CH$_3$OH	–	–	12 700.0 (1420.0)^b	2160.0 (257.0)	–	13.0	≲3981.0	≲1670.0
^{13}CH$_3$OH	70.4 (1.9)	14.0	602.6 (67.6)^c	103.0 (12.2)	–	13.0	≲758.6	≲317.7
NH$_2$CHO	$\sim$68^f	12.3 (0.6)	5.9 (0.6)	1.0 (0.1)	$\sim$19^f	8.7 (0.8)	2.5 (0.5)	1.0 (0.2)
C$_2$H$_3$CN	$\sim$70^f	9.1 (0.9)	5.1 (1.6)	0.9 (0.3)	$\sim$20^f	11.5 (3.2)	2.0 (1.3)	0.8 (0.5)
CH$_3$CCH	$\sim$68^f	61.1 (10.9)	262.4 (16.9)	44.9 (3.4)	$\sim$21^f	54.8 (5.5)	74.1 (12.3)	31.0 (5.8)
CH$_3^{13}$CCH	80.9 (2.2)	61.1	12.6 (3.9)^d	2.2 (0.7)	–	54.8	≲12.8	≲5.4
CH$_3$CHO-A	$\sim$69^f	5.4 (0.4)	49.0 (10.2)	8.4 (1.8)	$\sim$17^f	4.5 (1.0)	12.0 (9.1)	5.0 (3.8)
CH$_3$CHO-E	$\sim$72^f	6.5 (0.6)	15.9 (5.0)	2.7 (0.9)	$\sim$21^f	6.2 (1.0)	20.9 (8.5)	8.8 (3.6)
HC$_5$N	$\sim$66^f	32.1 (4.7)	3.5 (1.2)	0.6 (0.2)	$\sim$20^f	44.5 (19.1)	2.2 (1.8)	0.9 (0.8)
CH$_3$COOH-E	–	–	≲4.0	≲0.7	–	–	≲4.3	≲1.8
CH$_3$OCHO-A	$\sim$69^f	11.5 (1.0)	34.7 (7.4)	5.9 (1.3)	–	–	≲19.8	≲8.3
CH$_3$OCHO-E	$\sim$70^f	11.9 (1.1)	36.3 (7.4)	6.2 (1.3)	17.7 (2.1)	–	23.4 (10)^c	9.8 (4.2)
HCOCH$_2$OH	73.8 (0.9)	–	6.5 (5.6)^c	1.1 (1.0)	–	–	≲4.8	≲2.0
C$_2$H$_5$CN	$\sim$67^f	13.0 (1.0)	8.1 (1.6)	1.4 (0.3)	$\sim$18^f	8.7 (3.6)	4.8 (3.2)	2.0 (1.4)
(CH$_3$)$_2$O	$\sim$72^f	20.3 (1.2)	91.2 (10.0)	15.5 (1.6)	$\sim$19^f	15.8 (7.6)	63.1 (50.1)	26.4 (21.1)
C$_2$H$_5$OH	$\sim$68^f	5.3 (0.4)	44.7 (8.7)	7.6 (1.5)	18.6 (0.5)	–	25.1 (2.5)^d	10.5 (1.4)

Notes: $^a T_{\rm rot}$ derived from RDs or assumed for deriving molecular column densities. The assumed $T_{\rm rot}$ for the ^{13}C isotopologues of CH$_3$CCH and CH$_3$CN are taken from their other isotopologues. The assumed $T_{\rm rot}$ for CH$_3$OH and its ^{13}C isotopologue are taken from Requena-Torres et al. (2008). The $T_{\rm rot}$ quoted with uncertainties are determined from RDs. When $T_{\rm rot}$ is not listed then $T_{\rm rot} = 10$ K is assumed, which corresponds to an average value of the low $T_{\rm rot}$ component derived from other molecules by using RDs. ^{b}We have inferred from the ^{12}C/^{13}C ≲ 15, ^{14}N/^{15}N ≲ 280 and ^{16}O/^{18}O ≲ 186 isotopic ratios given in Table 4 that the column density of the most abundant isotopologues of these molecules are biased by opacity or self-absorption. Thus here we have derived the column density by using either the ^{18}O, ^{15}N or ^{13}C isotopologue for the respective velocity component and assuming ^{16}O/^{18}O = 250 or ^{14}N/^{15}N > 600 (W&R94) and if necessary our value ^{12}C/^{13}C = 21. For LOS+0.693, the SiO column density is derived from the ^{28}SiO isotopologue assuming ^{28}Si/^{30}Si = 18 derived for LOS−0.11. ^{c}Only one line of this molecule was detected. ^{d}Although several transitions of this molecule are detected, there is an insufficient dynamical range for $E_{\rm u}$ to derive the column density from a RD, so we have chosen one transition (see note cd in the online version of Tables 1 and 2), usually the less affected by opacity. ^{e}The observed transition is contaminated by the emission from an unknown molecular species. ^{f}This velocity is an average of different detected transitions. ^{g}These velocity ranges are chosen for deriving velocity-integrated intensities used in the molecular column density estimate. For LOS+0.693 we have used a velocity range for the ^{13}CS(2–1) line as it is affected by opacity or self-absorption. For the ^{15}N isotopologues of HNC and HCN, the velocity ranges are suitable for deriving ^{14}N/^{15}N ratios (see text).

of 2, to $\sim$5 × 10^4 cm^{-3}. The derived excitation temperatures are very sensitive to the H$_2$ density. Changes by a factor of 2 in the H$_2$ densities increase the excitation temperature from $\sim$14 to $\sim$24 K. The latter predicted temperature is inconsistent with our measured $T_{\rm rot}$ for HC$_3$N, ruling out higher H$_2$ densities in both GC sources.

3.4 Isotopic ratios

We have used the large number of detected isotopologues to derive from their column densities the isotopic ratios of ^{12}C/^{13}C, ^{14}N/^{15}N, ^{16}O/^{18}O, ^{18}O/^{17}O, ^{29}Si/^{30}Si and ^{32}S/^{34}S for both GC sources. Table 4 summarizes all the derived isotopic ratios based on optically thin emission (the unbiased group) and optically thick emission (the biased group). When possible, we have also used column densities of isotopologues with double isotopic substitution to guarantee optically thin emission. The canonical isotopic ratios derived for the GC by W&R94 are also shown in Table 4. As expected, the isotopic ratios of $\sim$3–15 derived from the biased group are always smaller than the canonical isotopic ratios due to the opacity effects for the most abundant isotopic substitution. The unbiased ^{12}C/^{13}C isotopic ratios derived for both GC sources are similar, within uncertainties, and the average, ^{12}C/^{13}C = 21.3 (1.7), is similar to the canonical value.

We also found ^{18}O/^{17}O = 3.7 (0.5) and ^{29}Si/^{30}Si = 1.7 (0.2) averaged over both GC sources, which are also similar to the canonical values within the uncertainties. Our lower limits for the ^{16}O/^{18}O and ^{14}N/^{15}N ratios are also consistent with the canonical values. The ^{32}S/^{34}S isotopic ratios derived for LOS+0.693 are lower than that found in W&R94, because the OC^{34}S lines are affected by ripples (see Fig. 2) and likely the OC^{34}S column density is over-estimated. However, for LOS−0.11 the lower limit of 22 for the OCS/OC^{34}S ratio is close to the canonical value. Our averaged ^{12}C/^{13}C, ^{18}O/^{17}O and ^{29}Si/^{30}Si isotopic ratios are similar to the canonical values (W&R94) within 1σ, which is $\sim$10 per cent of the derived isotopic ratios. This indicates that chemical isotopic fractionation and selective photodissociation are negligible, less than $\sim$10 per cent, for most of the molecules and the physical conditions in the GC, consistent with the results obtained by Riquelme et al. (2010).

The ^{12}C isotope is a primary product of nucleosynthesis in stellar cores, while the ^{13}C isotope is thought to be formed from ^{12}C present in stars of later generations (Wilson & Matteucci 1992). Thus, the ^{12}C/^{13}C ratio can be considered a measure of the degree of gas processing in the interstellar medium. Using CCH and its ^{13}C isotopologues, Martín et al. (2010) derived very large ^{12}C/^{13}C >138 and >81 towards the starburst galaxies M82 and NGC 253, respectively. Based on the hyperfine fits to the CCH line profiles, they ruled out opacity effects for the CCH lines. The ^{12}C/^{13}C ratio in the GC is at least a factor of 4 lower than in both starburst galaxies, suggesting that the degree of gas processing is quite different in them.
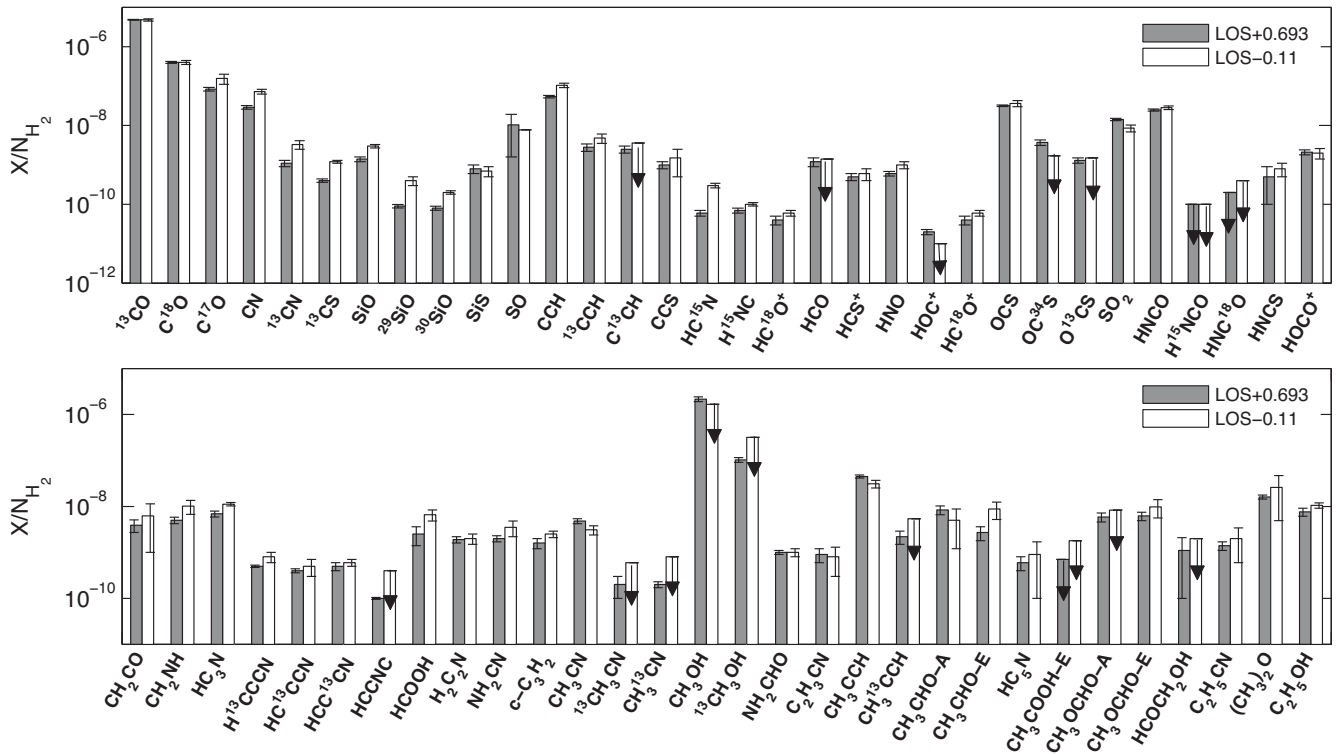
Figure 6. Abundances relative to H_2 for molecules detected in this survey. Arrows correspond to upper limits for the derived abundances. CH_3OH lines are observed in LOS−0.11, but we were able to derive only an upper limit for the CH_3OH column density (see Section 3.3.1).

4 DISCUSSION

4.1 Uniform molecular abundances and excitation conditions in the nuclei of galaxies

4.1.1 Galactic centre

Early studies of the distribution of the kinetic temperature in the molecular material in the GC using both ammonia and H_2 have shown that molecular clouds are warm with a mean $T_{kin} \approx 100$ K (Hüttemeister et al. 1993; Rodríguez-Fernández et al. 2001). More recently, Requena-Torres et al. (2006) found that the abundance of complex organic molecules is also relatively uniform in the molecular clouds in the GC. In agreement with the findings of Requena-Torres et al. (2006), we also found that the molecular clouds towards two LOSs, LOS+0.693 and LOS−0.11, separated by more than ∼120 pc within the GC, show a rather uniform chemistry. ∼80 per cent of molecular species detected in both LOSs show similar abundances within a factor of 2, even for the most complex organic molecules like C_2H_5OH, C_2H_5CN and $(CH_3)_2O$.

Our $(CH_3)_2O$, CH_3OH, $HCOOH$, $HNCO$, ^{13}CS and $C^{18}O$ abundances are also consistent with those derived in previous studies towards both GC sources from 2 and 3 mm line data (Requena-Torres et al. 2006; Martín et al. 2008). The uniform chemistry in the GC was explained for complex molecules as due to grain surface chemistry followed by the sputtering of the icy mantles by shocks. Our database can be used to give a detailed comparison of the excitation conditions found along the two LOSs. Fig. 7 shows the T_{rot} derived for LOS+0.693 versus the T_{rot} derived for LOS−0.11. It is remarkable that the excitation of the molecular gas is very similar for both GC sources. In fact, 86 per cent of the

molecules show the same T_{rot} within 1σ. Another two molecules (c-C_3H_2 and NH_2CHO) have T_{rot} that are consistent within 3σ. HC_3N is the only molecule with a significant difference above the 3σ level in its excitation between the GC sources. However, the difference in the T_{rot} by a factor of 1.4 corresponds to a change of only a factor of 1.8 in the derived H_2 densities of the molecular gas (see Section 3.3.4). The similar excitation conditions and molecular complexity found in the molecular gas in the two LOSs indicate that physical processes operating in the GC are widespread, driving the chemistry and affecting the physical conditions over large scales.

It is remarkable that complex organic molecules like CH_2CO, HC_5N, NH_2CN, CH_3CCH and CH_3CN have the largest T_{rot} in our survey. We do not believe the high temperatures derived for CH_2CO and NH_2CN are biased by the range of the energy levels of the observed transitions. Although the HNCO RDs (see Fig. 5) cover the same range of energies as NH_2CN, the derived T_{rot} for both molecules are very different. The wide range of derived T_{rot} for the different molecules does not seem to be due to differences in collisional cross-sections, level structure or dipole moments. For NH_2CN and CH_2CO, which have virtually identical geometrical cross-sections and level structure but very different dipole moments ($\mu_a = 4.32$ D for NH_2CN and $\mu_a = 1.414$ D for CH_2CO), one would expect to observe a larger T_{rot} for CH_2CO. In contrast, NH_2CN has a higher T_{rot} than CH_2CO.

Fig. 8 shows the molecular excitation (T_{rot}) derived for LOS+0.693 as a function of the dipole moment of the molecule. We found that there is no clear dependence of T_{rot} with the dipole moment as would be expected if the emissions from all molecules arise from the same region. Although the origin of the difference in T_{rot} is uncertain, we postulate that it may be related to the formation of the molecular species. In the shock scenario proposed by

Table 4. Isotopic ratios for both GC LOSs.

Isotope	Molecular column density ratio	LOS+0.693 V_{LSR} (km s^{-1}) $\sim$68	$\sim$85	LOS-0.11 V_{LSR} (km s^{-1}) $\sim$20	Bibliographic data[a]
	Ratios and limits unbiased by opacity or self-absorption for both GC sources				
^{12}C/^{13}C	CN:^{13}CN	22.9 (4.7)	–	21.2 (5.7)	$\sim$20
	CCH:^{13}CCH	19.1 (4.1)	–	22.6 (6.5)	
	CCH:C^{13}CH	21.4 (3.9)	–	$\gtrsim$29	
	OCS:O^{13}CS	22.8 (3.8)	–	$\gtrsim$25	
	CH$_3$CCH:CH$_3^{13}$CCH	20.8 (6.6)	–	$\gtrsim$6	
^{14}N/^{15}N	HNCO:H^{15}NCO	$\gtrsim$380	–	$\gtrsim$214	>600
^{18}O/^{17}O	C^{18}O:C^{17}O	4.8 (0.5)	–	2.6 (0.9)	3.2 (0.2)
^{16}O/^{18}O	HNCO:HNC^{18}O	$\gtrsim$129	–	$\gtrsim$78	250
^{29}Si/^{30}Si	^{29}SiO:^{30}SiO	1.1 (0.2)	–	2.2 (0.4)	1.5
	Ratios and limits biased by opacity, self-absorption or ripples for one or both GC sources				
^{12}C/^{13}C	HCN:H^{13}CN	4.5 (0.7)[b]	5.1 (0.7)	4.4 (0.1)[c]	$\sim$20
	HNC:HN^{13}C	3.0 (0.4)[b]	–	5.1 (0.3)	
	HCO$^+$:H^{13}CO$^+$	5.0 (0.7)[b]	6.8 (1.0)	7.1 (0.2)[c]	
	HC$_3$N:H^{13}CCCN	11.6 (0.8)	–	13.9 (2.4)	
	HC$_3$N:HC^{13}CCN	14.8 (1.5)	–	21.1 (6.1)	
	HC$_3$N:HCC^{13}CN	11.0 (2.1)	–	20.0 (4.7)	
	CH$_3$OH:^{13}CH$_3$OH	15.1 (3.8)	–	–	
	CH$_3$CN:^{13}CH$_3$CN	13.6 (9.1)	–	$\gtrsim$5	
	CH$_3$CN:CH$_3^{13}$CN	10.9 (1.6)	–	$\gtrsim$4	
^{14}N/^{15}N	^{12}C:^{13}C × HN^{13}C:H^{15}NC	148.7 (23.4)[d, e]	–	280.8 (25.2)[e]	>600
	^{12}C:^{13}C × H^{13}CN:HC^{15}N	100.5 (14.7)[d, e]	163.0 (23.1)[d]	141.8 (17.3)[e]	
^{16}O/^{18}O	^{12}C:^{13}C × ^{13}CO:C^{18}O	136.3 (7.2)[e]	–	185.5 (17.0)[e]	250
^{32}S/^{34}S	OCS:OC^{34}S	8.7 (1.3)[f]	–	$\gtrsim$22	$\sim$22
	^{12}C:^{13}C × O^{13}CS:OC^{34}S	7.7 (1.6)[e, f]	–	–	
	O^{13}CS:O^{13}C^{34}S	$\gtrsim$3	–	–	

Notes: [a]Isotopic ratios from W&R94. [b]The ^{12}C and ^{13}C isotopologues are affected by opacity or self-absorption. [c]The ^{12}C isotopologue is affected by opacity or self-absorption. [d]The ^{13}C isotopologue is affected by opacity or self-absorption. [e]We have averaged the ^{12}C/^{13}C isotopic ratios unbiased by opacity or self-absorption, then we have obtained the average ^{12}C/^{13}C $\sim$ 21 ratio over both GC sources. In these ratios we have used the ratio ^{12}C/^{13}C = 21. [f]The OC^{34}S lines are affected by ripples.
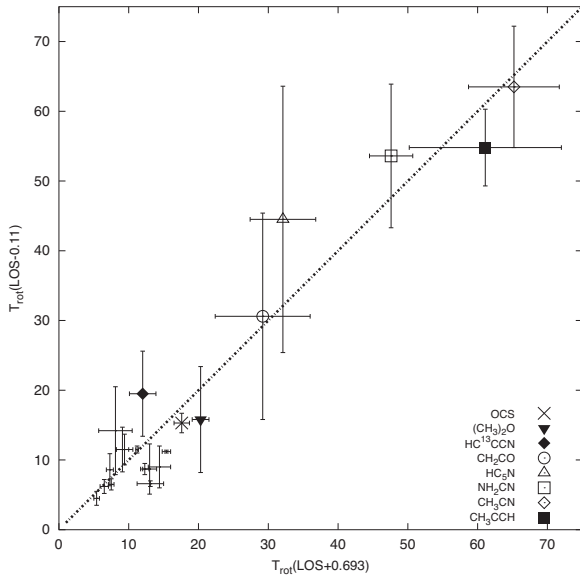
Figure 7. Relation between T_{rot} of both GC sources. The eight symbols show the highest T_{rot} measured for both GC sources. The dashed line shows the line of equal T_{rot}.
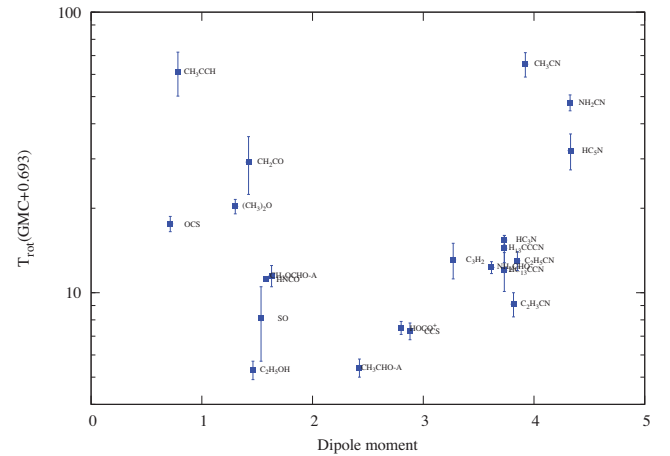
Figure 8. Molecular dipole moments as a function of T_{rot} derived for LOS+0.693. CH$_3$CN and CH$_3$CCH are the molecules that show the highest T_{rot} in this survey. When any molecule has more than one dipole moment, we have plotted the highest value.

Requena-Torres et al. (2006) and Martín et al. (2008), the molecular species with higher T_{rot} will be those produced at early times or just ejected from the grain, and those with lower T_{rot} should be located in the post-shocked regions.

Table 5. Abundance and excitation of Galactic and extragalactic sources.

Source name and nominal positions J2000 (α, β)	Type	Molecule	$T_{\rm rot}$ (σ) (K)	$N_{\rm H_2}$ (σ) (cm^{-2})	N (σ) ($\times 10^{13}$ cm^{-2})	$X = N/N_{\rm H_2}$ ($\times 10^{-9}$)	$(X_1/X)^A$
LOS+0.693 17$^{\rm h}$47$^{\rm m}$22$^{\rm s}$0 $-$28°21′27″0	Molecular cloud	CS	10.0	5.9 (0.2) × 10^{22}	48.3 (4.2)^B	8.2 (1.0)	3.0 (0.4)
		SO	8.1 (2.4)		61.0 (51.3)	10.3 (8.7)	0.8 (0.6)
		SiO	10.0		9.0 (1.8)	1.4 (0.2)	2.1 (0.3)
		OCS	17.6 (1.1)		186.2 (4.6)	31.6 (1.5)	1.2 (0.2)
		CCH	10.0		316.2 (18.6)	53.6 (3.8)	2.0 (0.3)
		HCO$^+$	10.0		57.0 (1.3)	9.6 (2.2)	1.6 (0.5)
		HNCO	11.2 (0.2)		144.5 (5.6)	24.5 (1.3)	1.2 (0.1)
		HC$_3$N	15.4 (0.6)		54.9 (3.3)	9.4 (1.0)	1.2 (0.1)
		CH$_3$OH	14.0 (1.3)^a		12 700.0 (1420.3)	2160.0 (255.0)	0.5 (0.1)
		CH$_3$CCH	61.1 (10.9)		262.4 (16.9)	44.5 (3.3)	0.7 (0.1)
LOS$-$0.11 17$^{\rm h}$45$^{\rm m}$39$^{\rm s}$0 $-$29°04′05″0	Molecular cloud	CS	10.0	2.4 (0.2) × 10^{22}	58.8 (2.1)^B	24.5 (2.2)	1
		SO	14.2		18.6 (3.7)	7.8 (2.0)	1
		SiO	10.0		7.2 (0.2)	3.0 (0.3)	1
		OCS	15.3 (1.4)		87.1 (14.1)	36.3 (6.6)	1
		CCH	10.0		251.2 (24.0)	104.7 (13.2)	1
		HCO$^+$	10.0		36.0 (0.8)	15.5 (3.0)	1
		HNCO	11.5 (0.5)		67.6 (4.5)	28.2 (3.0)	1
		HC$_3$N	11.2 (0.2)		26.8 (0.6)	11.2 (1.0)	1
		CH$_3$OH	13.0 (1.0)^a		–	1100.0 (220)$^{a, C}$	1
		CH$_3$CCH	54.8 (5.5)		74.1 (12.3)	30.9 (5.7)	1
NGC 253 00$^{\rm h}$47$^{\rm m}$33$^{\rm s}$3 $-$25°17′23″0	Intermediate-age starburst	CS	12.0 (3)^b	6.2 (0.5) × 10^{22b}	15.0 (6.0)^b	2.4 (1.0)	10.2 (4.2)
		SO	40 (24)^c		4.5 (3.3)^c	0.73 (0.5)	10.7 (7.9)
		SiO	7.4 (0.7)^c		0.5 (0.1)^c	0.081 (0.02)	37.0 (8.7)
		OCS	17 (2)^c		25.0 (3.0)^c	4.0 (0.6)	9.1 (2.0)
		CCH	10.0^d		73.0 (1.0)^d	11.8 (1.0)	8.9 (1.3)
		HNCO	23.0 (6.0)^c		5.7 (2.7)^c	0.9 (0.4)	31.3 (15.0)
		HC$_3$N	11.6 (1.8)^b		8.1 (2.9)^b	1.3 (0.5)	8.6 (3.2)
		CH$_3$OH	11.6 (0.2)^c		83 (3)^c	13.4 (1.2)	82.1 (18.0)
		CH$_3$CCH	44.4 (7.7)^b		32.0 (10.0)^b	5.2 (1.7)	5.9 (2.2)
M82 09$^{\rm h}$55$^{\rm m}$51$^{\rm s}$9 69°40′47″1	Evolved starburst	CS	15.1 (0.9)^b	7.9 (0.4) × 10^{22b}	3.6 (0.5)^b	0.5 (0.1)	49.0 (9.3)
		CCH	10.0$^{e, D}$		55.0 (1.0)$^{e, D}$	6.5 (0.4)^D	16.1 (2.2)
		HNCO	10.0$^{f, D}$		≲0.7$^{f, D}$	≲0.1^D	≳282
		HC$_3$N	24.7 (3.9)^b		2.5 (1.1)^b	0.3 (0.1)	37.3 (16.0)
		CH$_3$OH	4.5^f		15.0^f	1.9	579.0
		CH$_3$CCH	28.1 (1.2)^b		85.0 (9.0)^b	10.8 (1.3)	2.9 (0.6)
IC 342 03$^{\rm h}$46$^{\rm m}$48$^{\rm s}$5 68°05′46″0	Intermediate-age starburst	CS	10.6 (0.2)^b	5.8 (0.4) × 10^{22b}	6.0 (0.1)^b	1.0 (0.1)	24.5 (2.6)
		SO	–		–	≳0.08$^{g, E}$	≳1.1
		CCH	–		–	0.3$^{g, E}$	3.5
		HNCO	10.2 (0.4)^e		12.0 (1.0)^e	2.1 (0.2)	13.4 (2.0)
		HC$_3$N	13.1 (2.3)^b		2.7 (1.1)^b	0.5 (0.2)	22.4 (10.0)
		CH$_3$OH	–		–	5$^{g, E}$	220
		CH$_3$CCH	70.0^b		45.0^b	7.8	4.0
Maffei 2 02$^{\rm h}$41$^{\rm m}$55$^{\rm s}$1 59°36′15″0	Young starburst	CS	9.7 (8.1)^b	4.4 (0.8) × 10^{22b}	6.9 (5.7)^b	1.6 (1.3)	15.3 (13.3)
		SiO	–		–	0.08$^{h, E}$	36.2
		CCH	–		–	9.6$^{h, E}$	10.9
		HCO$^+$	–		–	3.5$^{h, E}$	4.4
		HNCO	11.5 (0.6)^e		10 (2)^e	2.3 (0.6)	12.3 (3.6)
		HC$_3$N	11.6 (0.8)^b		4.3 (0.6)^b	1.0 (0.2)	11.2 (2.8)
		CH$_3$OH	10.0^f		33.0^f	7.5	147.0
		CH$_3$CCH	≲46.9^b		≲11^b	≲2.5	≳12.4

Notes. (A) Ratio between the molecular abundances for LOS$-$0.11 and those for the other sources in this table. (B) The CS abundances for both GC sources are derived from the ^{13}CS abundances by using our ^{12}C/^{13}C = 21 ratio. (C) An uncertainty of 20 per cent in the methanol abundance is assumed. (D) Offset position of 13″0, 7″5 relative to 09$^{\rm h}$55$^{\rm m}$51$^{\rm s}$9, 69°40′47″1 (J2000) with $N_{\rm H_2}$ = 8.5 × 10^{22} cm^{-2} (Martín, Martín-Pintado & Mauersberger 2006a). (E) This abundance corresponds to cloud A in IC 342 or cloud F in Maffei 2; both clouds are located in projection close to the nuclear star clusters. Uncertainties in the abundances are at least a factor of 3. ^{a}Requena-Torres et al. (2008). ^{b}Aladro et al. (2011a). ^{c}Martín et al. (2006b). ^{d}Martín et al. (2010). ^{e}Martín et al. (2009a). ^{f}Martín, Martín-Pintado & Mauersberger (2006a). ^{g}Meier & Turner (2005). ^{h}Meier & Turner (2012).

4.1.2 Starburst galaxies

The bulk of the quiescent molecular clouds in the GC seem to show rather uniform physical conditions and chemical composition. In

this section we compare our results obtained for the GC clouds with those derived for nearby extragalactic nuclei with a different type of activity. Table 5 summarizes the $T_{\rm rot}$ and molecular abundances of selected species derived for both GC sources and four

extragalactic nuclei, NGC 253, M82, IC 342 and Maffei 2. The molecular species selected in Table 5 and their corresponding T_{rot} has been successfully used by Martín, Martín-Pintado & Mauersberger (2009a) and Aladro et al. (2011a) to study the evolution of the nuclei of starburst galaxies. Based on the excitation and the molecular abundances, Martín et al. (2009a) and Aladro et al. (2011a) have classified Maffei 2 as a young starburst galaxy, IC 342 and NGC 253 as intermediate-age starburst galaxies and M82 as an evolved starburst galaxy (Aladro et al. 2011a).

In column 8 of Table 5, we show the ratio between the molecular abundances of LOS−0.11 relative to those of LOS+0.693 and the nuclei of nearby galaxies. While the molecular abundances in the two GC LOSs clouds are within a factor of 3, those in galactic nuclei are, for most molecules, at least 1 order of magnitude smaller than those measured in the GC. This is expected since the volume sampled in external galaxies is, at least, 4 orders of magnitude larger than in the GC. Thus, the ratios between diffuse molecular gas measured by the H_2 column densities and dense gas traced by other species are smaller in the GC than in external galaxies. However, some molecular species show changes in their abundances by more than 1 order of magnitude relative to high-density tracers like CS. In particular, CH_3OH has the lowest abundances in galaxies like M82, IC 342 and Maffei 2 by factors of $\sim(1-6) \times 10^2$ relative to LOS−0.11. NGC 253 is the galaxy with the highest methanol abundance of the starburst galaxies in our sample. The radiation field in NGC 253 seems to be higher than in M82, IC 342 and Maffei 2 (Carral et at. 1994; Israel & Baas 2003). However, differences in the evolutionary stage of the starbursts and molecular clouds (Aladro et al. 2011a), the distribution of star-forming regions and/or the strength of large-scale shocks could be responsible for the high methanol abundance in NGC 253 compared to those of the other galaxies in our sample. Similar lower methanol abundances, by nearly 2 orders of magnitude, are also observed towards a sample of molecular clouds in the GC (Requena-Torres et al. 2006) that are affected by the UV photodissociation from H II regions. This suggests that this molecule is likely photodissociated by the strong UV radiation field of $G_0 \sim 10^{2.5 - 4.0}$ (Carral et at. 1994; Israel & Baas 2003) present in these nearby galaxies considered in this comparison.

Another molecule that also shows large abundance differences between our sample of galaxies and LOS−0.11 is HNCO. It is expected that gas-phase HNCO survives in well-shielded dense molecular clouds, while it is photodissociated in unshielded regions affected by UV radiation (Martín et al. 2008). The high HNCO abundances derived for both GC sources compared to those found for the starburst galaxies NGC 253 and M82 support the idea that HNCO is a suitable tracer of dense molecular gas ($\gtrsim 10^6$ cm^{-3}) in clouds unaffected by strong UV radiation (Martín et al. 2008). This agrees with the finding of Amo-Baladrón et al. (2011), who found that the HNCO abundance in the 20 km s^{-1} cloud dominated by shocks is a factor of 20 higher than in the circumnuclear disk surrounding Sgr A*, which is affected by both shocks and photodissociation.

The photodissociation rate of HNCO is a factor of ~ 1.5 larger than that of CH_3OH. Both molecules have photodissociation rates higher (a factor ~ 3) and lower (a factor ~ 4) than those of CCH and HC$_3$N, respectively. The smaller differences found for the CCH abundances compared to those of CH_3OH and HNCO between LOS−0.11 and the starburst galaxies M82 and NGC 253 is likely due to the differences in the photodissociation rates of these molecules. Additionally, the abundance of CCH could increase efficiently in PDRs (Mul & McGowan 1980). One expects that HC$_3$N would show larger abundance variations than CH_3OH and HNCO

between LOS−0.11 and both starburst galaxies due to the differences in the photodissociation rates. However, this is not observed in Table 5. Efficient formation of HC$_3$N through ion-molecule chemistry (Knight et al. 1986) could be responsible for the high HC$_3$N abundance found in both starburst galaxies. The largest differences shown by CH_3OH and HNCO in our comparison is likely due to their photodissociation and that both molecules are not expected to form efficiently in the gas phase. Between LOS−0.11 and the starburst galaxies in our sample, the differences in the abundance of CH_3OH are higher than for HNCO. This is probably due to the higher extinction of the dense cloud cores where HNCO arises ($\gtrsim 10^6$ cm^{-3}) (Martín et al. 2008) compared with the more diffuse conditions where CH_3OH is found ($\sim 5 \times 10^4$ cm^{-3}) (Martín, Martín-Pintado & Mauersberger 2006a).

Overall, the complex molecules in the molecular clouds of this sample of starburst galaxies have smaller abundances than those measured in the GC sources by nearly 2 orders of magnitude, suggesting that a substantial fraction of the molecular gas in the nearby galaxies in our sample is affected by photodissociation by the UV radiation from the starburst.

Fig. 9 shows the T_{rot} of selected molecules derived for NGC 253 (Martín et al. 2006b; Aladro et al. 2011a) and M82 (Aladro et al. 2011b) versus the T_{rot} derived for LOS−0.11. In contrast to the large abundance difference found between the GC clouds and starburst galaxies, the excitation of complex molecules like c-C$_3$H$_2$, HC$_3$N and CH_3OH derived for both starburst galaxies, NGC 253 and M82, is similar within $\sim 3\sigma$ to the excitation of the molecular cloud found for LOS−0.11. As for the two LOSs in the GC, NH$_2$CN and CH$_3$CCH in NGC 253 also show high $T_{rot} = 67$ and 44 K, respectively. Interestingly these T_{rot} are within a factor of 1.2 of those of NGC 253. For M82, the T_{rot} derived for CH$_3$CCH and CH$_3$CN show the same trend as for NGC 253 but in this case they are a factor of ~ 2 lower than those observed for LOS−0.11. It is remarkable that the excitation of molecular clouds in the nuclei of galaxies with different activities and evolutionary stages appears relatively uniform, suggesting that the physical conditions, H_2 densities and kinetic temperatures must be very similar. If, as suggested in the previous section, the excitation of the molecules is related to the formation mechanism, there must be common processes driving the chemistry in the nuclei of galaxies. However, to explain the underabundance of CS, HC$_3$N, CH_3OH, HNCO and other molecules (see Table 5) found in our sample of galactic nuclei with respect to the GC, the shock scenario proposed by Requena-Torres et al. (2006) and Martín et al. (2008) for the GC must be combined with the effects of the photodissociation proposed by Aladro et al. (2011b).

4.2 Tracing the UV- and X-ray-induced chemistry in galactic nuclei

The scenario proposed in the previous section to explain the difference in abundance ratios between these quiescent GC LOSs and our sample of galactic nuclei would indicate that the clouds in the two LOSs are only marginally affected by the UV radiation. However, in our survey we have detected, for the first time, HCO and HOC$^+$ emission towards LOS+0.693 in the GC. Emissions from these molecules are considered to be tracers of UV- and X-ray-induced chemistry in the associated PDRs (Apponi et al. 1999; Goicoechea et al. 2009; Martín et al. 2009b) and XDRs (Usero et al. 2004; Spaans & Meijerink 2007). It has been proposed that abundance and abundance ratios between key molecules like HCO, HOC$^+$ and HCO$^+$ can be used to trace the XDR and PDR chemistries and even
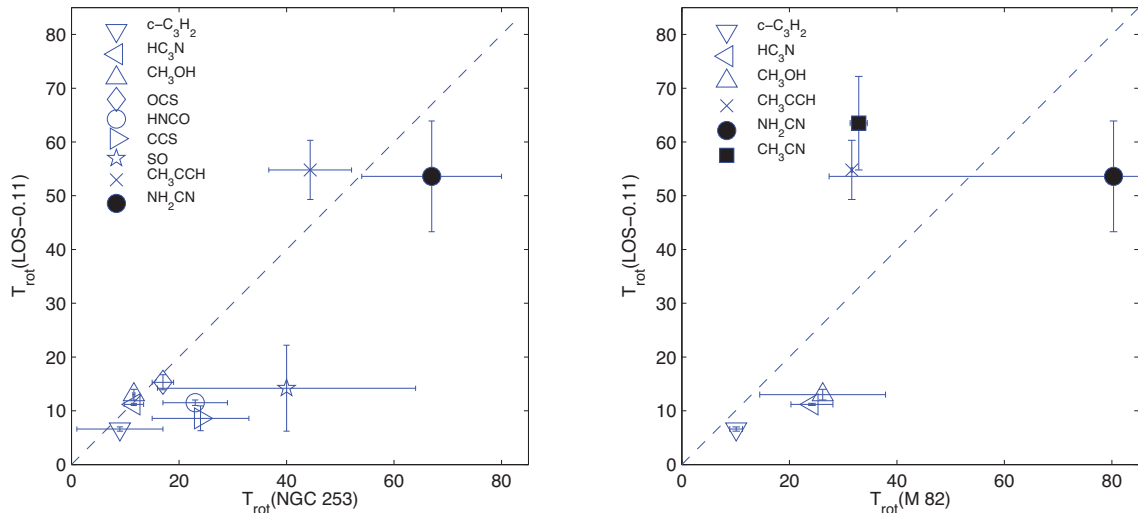
Figure 9. Relation of the $T_{\rm rot}$ of NGC 253 (left) and M82 (right) with the $T_{\rm rot}$ of LOS$-$0.11. Different symbols correspond to different molecules. The $T_{\rm rot}$ for NGC 253 are taken from Martín et al. (2006b) and Aladro et al. (2011a), and for M82 from Aladro et al. (2011b). For LOS$-$0.11, the $T_{\rm rot}$ of methanol is taken from Requena-Torres et al. (2008). The dashed line on each plot is the line of equal $T_{\rm rot}$.

to differentiate between them (Meijerink, Spaans & Israel 2007; Spaans & Meijerink 2007). The high spatial resolution of our data offers a unique opportunity to study the PDR/XDR component in nuclei of galaxies using molecular tracers.

4.2.1 Constraints on the X-ray radiation in the molecular clouds along the GC LOS

Fig. 10 illustrates the key difference in the X-ray emissions observed towards the two LOSs (shown as open circles) in the GC. While LOS$-$0.11 shows continuum emission only in the 0.1–10 keV band, LOS+0.693 shows, in addition to the continuum emission, one of the strongest Fe Kα (6.4 keV) lines observed in our Galaxy (Koyama et al. 1996). The presence of the strong Fe Kα line emission is considered as an excellent tracer of XDRs (Martín-Pintado et al. 2000), showing that X-rays are directly interacting with large column densities of matter. As a consequence of this interaction, one would expect a chemistry driven by X-rays. In contrast, LOS$-$0.11 does not show any emission of the Fe Kα line (Ponti et al. 2010), indicating the lack of any relevant XDR.

4.2.2 Constraints on the UV radiation in the molecular clouds along the GC LOS

As shown in Fig. 1, the two LOSs do not have any prominent H II regions that could produce associated PDRs. However, LOS+0.693 is relatively close to the H II regions of Sgr B2N and L, whereas LOS$-$0.11 is located near the non-thermal sources Sgr A-E and Sgr-F (Lu et al. 2003; Yusef-Zadeh et al. 2005). We can use the upper limit for the Hα recombination line emission in our survey to constrain the Lyman photons in the beam. None of the four recombination lines, Hα and H39α to H43α, that fall in the frequency range of our spectral line survey are detected towards both LOSs. From the 3σ upper limit for their intensities and assuming a linewidth of $\sim$35 km s^{-1}, we have set the upper limits of the thermal continuum fluxes given in Table 6. For optically thin emission and the average LTE electron temperature of 6500 K estimated for the GC (Goss et al. 1985), we have derived the upper limits of the Lyman continuum photons (Mezger & Henderson 1967) given in Table 6. These upper limits of $\lesssim 10^{48.4}$ and $\lesssim 10^{48.7}$ s^{-1} for LOS+0.693 and

LOS$-$0.11, respectively, would constrain the spectral type of any ionizing star to be later than O8-O9.

Low-angular-resolution observations of fine structure lines of C II and O I towards Sgr B2 have shown the presence of an extended far-UV (FUV) radiation field of $G_0 \approx 10^3$–10^4, which should produce important PDRs. However, this FUV radiation field would be characterized by a Lyman continuum photon flux of $\sim$10$^{50.4}$ s^{-1} (Goicoechea et al. 2004). This flux is $\sim$50 times larger than that derived for LOS+0.693 from the recombination lines. Given the large difference in beam size between our observations and those of the fine structure lines, it is possible that inhomogeneities in the FUV radiation field could partially explain this discrepancy. In any case, the UV radiation field strength of the PDR component in LOS+0.693 is rather uncertain. The situation for LOS$-$0.11 seems to be simpler since there is no nearby massive star formation, like Sgr B2N, which could provide a large FUV radiation field. For this LOS, one expects a negligible PDR component.

4.2.3 HCO, HOC$^+$, HCO$^+$ and CS abundances as tracers of the PDR and XDR components in galactic nuclei

Table 7 shows the HCO$^+$/HOC$^+$, HCO$^+$/HCO and HCO/HOC$^+$ ratios measured for our two LOSs, extragalactic sources (NGC 253, M82 and NGC 1068) and typical galactic PDRs. The HCO$^+$ column densities are calculated from the HC^{18}O$^+$ line by assuming ^{16}O/^{18}O = 250 (W&R94). We also have included abundances of CS relative to HOC$^+$ and HCO since the CS abundance does not seem to change substantially in PDRs and shocked environments in the GC (Requena-Torres et al. 2006; Martín et al. 2008).

4.2.4 CS/HOC$^+$ and CS/HCO ratios

Both LOSs in the GC show CS/HOC$^+$ ratios that are larger than those measured for Galactic PDRs and galaxies by factors of $\gtrsim$4 and $\gtrsim$15, respectively, except for that of the molecular peak of the Orion Bar, which is completely shielded from UV radiation. Although the CS/HCO ratios also show the same trend as CS/HOC$^+$, the CS/HCO ratios are less conclusive since they are within a factor of $\sim$3 for all kinds of objects. This suggests that the PDR/XDR component, traced by HOC$^+$ and to a lesser extent by HCO in
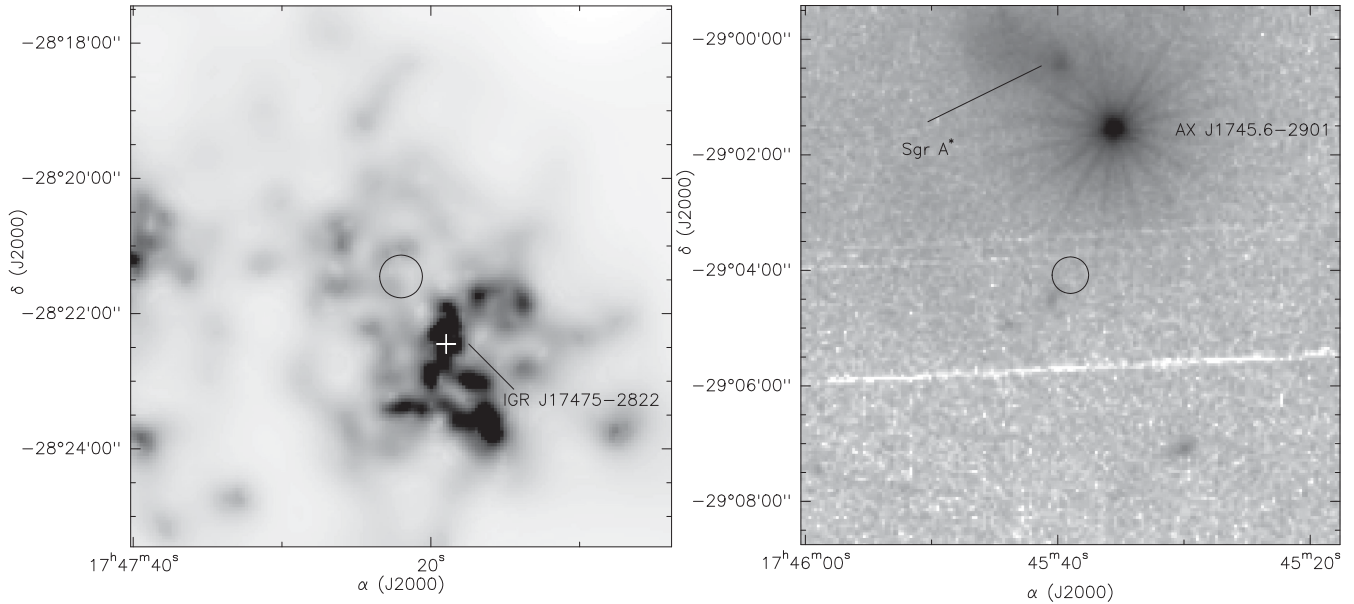
Figure 10. (Left panel) Fe Kα line emission observed with the *XMM-Newton* satellite in 2001–2004 towards Sgr B2 (Terrier et al. 2010). The white cross shows the position of the X-ray source IGR J17475-2822. (Right panel) 0.1–10 keV image observed with *XMM-Newton* in April 2007 towards Sgr A (image taken from http://xmm.esac.esa.int/xsa/index.shtml). The line shows the position of Sgr A*. AX J1745.6-2901 is the brightest source in the field. The circles with the beam size of the Mopra telescope (38 arcsec at 90 GHz) show LOS+0.693 and LOS−0.11 in the left and right panels, respectively.

Table 6. Physical parameters derived from Hα recombination lines.

Recombination line	ν (GHz)	LOS+0.693			LOS−0.11		
		Continuum flux (Jy)	Electron density (cm^{-3})	Flux of Lyman continuum photons $\log(N_{\rm Lyc})$ (s^{-1})	Continuum flux (Jy)	Electron Density (cm^{-3})	Flux of Lyman continuum photons $\log(N_{\rm Lyc})$ (s^{-1})
H43α	79.912	–	–	–	$\lesssim$1.2	$\lesssim$473.2	$\lesssim$48.6
H42α	85.688	$\lesssim$1.4	$\lesssim$513.0	$\lesssim$48.7	$\lesssim$2.6	$\lesssim$715.9	$\lesssim$49.0
H41α	92.034	$\lesssim$1.5	$\lesssim$531.2	$\lesssim$48.7	$\lesssim$1.2	$\lesssim$480.5	$\lesssim$48.6
H39α	106.737	$\lesssim$0.8	$\lesssim$391.2	$\lesssim$48.4	$\lesssim$1.3	$\lesssim$501.5	$\lesssim$48.7

both LOSs of the GC, is smaller than those in starburst galaxies and typical unshielded galactic PDRs. The larger CS/HOC$^+$ ratio found for LOS−0.11 compared to LOS+0.693 suggests a very small (basically negligible) XDR/PDR component along LOS-0.11. This is consistent with the measurements of UV and X-ray emission towards these LOSs shown in Figs 1 and 10, respectively. The CS/HOC$^+$ ratios measured for external galaxies are also consistent with this ratio being a good tracer of the PDR/XDR component relative to the total gas (see Table 7). The most evolved starburst, M82, has the lowest CS/HOC$^+$ ratio (1), consistent with its classification as a PDR-dominated galaxy, while NGC 253, an intermediate-age starburst, has a larger CS/HOC$^+$ ratio of 25. The intermediate CS/HOC$^+$ ratio of 6 found for NGC 1068, which is considered to be dominated by X-ray chemistry, is much smaller than the ratio found for LOS+0.693, which also emits X-rays, suggesting that the CS/HOC$^+$ ratio could also be a good tracer of strong XDR components since the X-ray luminosity of NGC 1068 (Iwasawa, Fabian & Matt 1997) is nearly 4 orders of magnitude higher than for Sgr B2 (Koyama et al. 1996).

4.2.5 HCO$^+$/HOC$^+$ and HCO$^+$/HCO ratios

The abundance ratios HCO$^+$/HOC$^+$ and HCO$^+$/HCO have also been used to estimate the contribution of UV radiation to the chem-

istry of molecular clouds. HCO$^+$/HOC$^+$ ratios of <166 and 75–200 were measured for the Orion Bar (Fuente et al. 2003) and the Horsehead (Goicoechea et al. 2009), respectively, considered prototypical galactic PDRs. We found much larger HCO$^+$/HOC$^+$ ratios of 546 (175) and $\gtrsim$1134 for LOS+0.693 and LOS−0.11, respectively. These HCO$^+$/HOC$^+$ ratios are also higher than those measured for extragalactic sources. As for the CS/HOC$^+$ ratio, we found that the HCO$^+$/HOC$^+$ ratio of the molecular peak for the Orion Bar, as well as that of NGC 2023, are close to the values observed in the GC. We consider NGC 2023 to represent the conditions in a prototypical giant molecular cloud, since Savage & Ziurys (2004) claimed that the PDR observed is probably embedded in the molecular cloud, therefore the HCO$^+$/HOC$^+$ ratio would be biased towards that of a typical cloud unaffected by UV radiation.

The HCO$^+$/HCO ratios show the same trend as the HCO$^+$/HOC$^+$ ratios. The HCO$^+$/HCO ratios are factors of 4–8 (LOS+0.693) and $\gtrsim$5–10 (LOS−0.11) higher than the HCO$^+$/HCO ratio of 1–2 for typical galactic PDRs. However, it is not clear why there are smaller differences between both GC sources and galaxies for the HCO$^+$/HCO ratios. In our comparison, the PDRs NGC 7023 and NGC 2023 have the highest HCO$^+$/HCO ratios, which are biased because both sources were observed towards positions where the HCO$^+$ emission arises from shielded molecular clouds (Schilke et al. 2001; Savage & Ziurys 2004).

Table 7. Ratios for HCO$^+$, CS, HOC$^+$ and HCO.

Source	Velocity (km s^{-1})	HCO$^+$/HOC$^+$	HCO$^+$/HCO	HCO/HOC$^+$	CS/HCO	CS/HOC$^+$
LOS+0.693	∼68	546 (175)[a]	9 (3)[a]	62.9 (30.1)	6 (1)	378 (43)
LOS−0.11	∼20	≳1134[b]	≳11[b]	–	≳18	≳1960
NGC 253	∼180	80 (30)[c]	5.2 (1.8)[c]	15.4 (7.9)	2 (1)[d]	25 (10)[d]
	∼280	63 (17)[c]	5.4 (1.3)[c]	11.7 (4.2)	1.1 (0.5)[d]	13 (5)[d]
M82	∼310	60 (28)[c]	9.6 (2.8)[c]	6.3 (3.4)	1[e]	1[f]
NGC 1068	∼1100	128 (28)[c]	3.2 (1.2)[c]	40.0 (17.4)	0.3 (0.2)[g]	6 (4)[g]
Horsehead	–	75–200[h]	1.1[i]	68.2–181.8	–	–
Orion Bar (PDR peak)	∼9.5	<166[j]	2.4[k]	<69.2	3[l]	100[m]
Molecular peak	∼10.4	400[j]	–	–	–	4286[m]
NGC 7023 (PDR peak)	∼2.7	50–120[j]	31[k]	1.6-3.9	2[n]	66[o]
Molecular peak	–	>200[j]	–	–	–	≳61[o]
NGC 2023	∼10.0	1913[p]	12[k]	159.4	–	–
Diffuse clouds	–	70–120[q]	–	–	–	–

[a]We have derived $N_{HCO+} = 5.7\ (1.3) \times 10^{14}$ cm^{-2} from $N_{HC^{18}O+}$ assuming $^{16}O/^{18}O = 250$ (W&R94). We also have found $N_{HOC+} = 1.1\ (0.1) \times 10^{12}$ cm^{-2} and $N_{HCO} = 6.9(1.4) \times 10^{13}$ cm^{-2} for LOS+0.693. [b]We have derived $N_{HCO+} = 3.6\ (0.8) \times 10^{14}$ cm^{-2} from $N_{HC^{18}O+}$ assuming $^{16}O/^{18}O = 250$ (W&R94). We also have found $N_{HOC+} \lesssim 0.3 \times 10^{12}$ cm^{-2} and $N_{HCO} \lesssim 3.3 \times 10^{13}$ cm^{-2} for LOS−0.11. [c]Martín et al. (2009b). [d]Estimated from Martín et al. (2006b, 2009b). [e]Estimated from García-Burillo et al. (2002) and Aladro et al. (2011a). [f]Estimated from Fuente et al. (2006) and Aladro et al. (2011a). [g]Estimated from Martín et al. (2009a) and Aladro et al. (2013). [h]Goicoechea et al. (2009). [i]Gerin et al. (2009). [j]Fuente et al. (2003). [k]Schilke et al. (2001). [l]Estimated from Jansen et al. (1995) and Schilke et al. (2001). [m]Estimated from Jansen et al. (1995) and Fuente et al. (2003). [n]Estimated from Fuente et al. (1993) and Schilke et al. (2001). [o]Estimated from Fuente et al. (1993, 2003). [p]Savage & Ziurys (2004). [q]Liszt, Lucas & Black (2004).

The differences found for the HCO$^+$/HOC$^+$ and HCO$^+$/HCO ratios between our sample of typical PDRs and LOS+0.693 could be due to X-ray-induced chemistry in the giant XDR observed towards Sgr B2 in the Fe Kα (6.4 keV) line. It has been claimed that the HOC$^+$ and HCO abundances might increase in regions illuminated by X-rays. Usero et al. (2004) argued that XDR chemistry could provide an explanation for the different abundances of HCO$^+$ and HOC$^+$ measured in the circumnuclear disk of the active galactic nucleus NGC 1068, which also shows a strong Fe Kα (6.4 keV) line, like LOS+0.693. However, they found HCO$^+$/HOC$^+$ ∼ 40–100 and HCO$^+$/HCO = 3 in the circumnuclear disk of NGC 1068, which are similar to those found in our sample of typical PDRs. Therefore, XDR chemistry seems unlikely to explain the large HCO$^+$/HOC$^+$ and HCO$^+$/HCO ratios observed for the GC LOSs.

Meijerink et al. (2007) modelled the chemistry induced by PDRs and XDRs in clouds with different hydrogen column densities and incident FUV/X-ray radiation fields. Using these models, they predicted column density ratios for several molecules, including HCO$^+$/HOC$^+$ and HCO$^+$/HCO. For a hydrogen column density of ∼2 × 10^{21} cm^{-2} and $G_0 = 10^3$, the PDR model predicts HCO$^+$/HOC$^+$ ∼ 100, which agrees with those derived for NGC 7023 and the Orion Bar (Fuente et al. 2003). For an X-ray flux of 1.6 erg cm^{-2} s^{-1} and a density of 10^4 cm^{-3}, appropriate to LOS+0.693, the XDR models of Meijerink et al. (2007) predict HCO$^+$/HOC$^+$ ∼ 10 in the cloud interior. The predicted ratio is at least a factor of 55 lower than those inferred for both GC sources (see Table 7), indicating that XDR models cannot reproduce the observed HCO$^+$/HOC$^+$ ratios found for both GC sources. This result is consistent with the lack of X-ray emission from LOS−0.11 (see Fig. 10). HCO/HOC$^+$ ∼ 63 derived for LOS+0.693 cannot be used to distinguish between the XDR or PDR scenario since this ratio is close to those of both the Horsehead, a typical PDR, and the claimed XDR NGC 1068. Finally, HCO$^+$/HCO ∼1 predicted by Meijerink et al. (2007) for PDRs with $G_0 = 10^3$ is consistent with those for

the Horsehead and the Orion Bar (Gerin et al. 2009; Schilke et al. 2001).

In summary, as discussed throughout this section, the large HCO$^+$/HOC$^+$, CS/HOC$^+$ and HCO$^+$/HCO ratios suggest that the molecular gas affected by X-ray/UV radiation fields in the two GC LOSs represents a small fraction of the total column density of molecular gas. Assuming that the observed HCO$^+$/HCO = 1.1 for the Horsehead represents the actual PDR ratio, we estimated that roughly ∼12 per cent of the total column density would be affected by the UV radiation in LOS+0.693 and ≲10 per cent in LOS−0.11. These results also support the HNCO/CS diagnostic diagram proposed by Martín et al. (2008, 2009a) to establish the dominant chemistry and the heating mechanism working in molecular clouds, since by using this diagram they found that the chemistry and likely the heating of both GC sources are mainly dominated by shocks.

5 CONCLUSIONS

We used the Mopra telescope to carry out a 3-mm spectral line survey in the selected frequency ranges ∼77–93 GHz and ∼105–113 GHz of two LOSs, LOS+0.693 and LOS−0.11, towards the Sgr B2 and Sgr A complexes in the GC. The main conclusions of our study are the following:

(i) We detected 38 molecular species and 25 isotopologues in LOS+0.693 and 34 molecular species and 18 isotopologues in LOS−0.11. We detected for the first time the PDR/XDR tracers HCO and HOC$^+$ in the quiescent gas in LOS+0.693. These two species and the complex organic molecules HC$_2$NC and HCOCH$_2$OH were not detected towards LOS−0.11.

(ii) The molecular excitation T_{rot} and the molecular column densities were derived for all detected molecules using a LTE approximation. The derived T_{rot} varies between ∼5 and 73 K for both GC sources, but most molecules show T_{rot} < 20 K, indicating

subthermal excitation. The symmetric rotors, CH_3CN, $^{13}CH_3CN$ and CH_3CCH, have the highest $T_{rot} \sim 55$–73 K, consistent with $T_{kin} \sim 100$ K previously derived for the GC clouds.

(iii) Although LOS+0.693 and LOS−0.11 are separated by more than ~ 120 pc within the GC, ~ 80 per cent of molecular species detected in both GC sources have similar abundances, within a factor of 2, and similar excitation conditions.

(iv) We used the large number of detected isotopologues to derive isotopic ratios for $^{12}C/^{13}C$, $^{14}N/^{15}N$, $^{16}O/^{18}O$, $^{18}O/^{17}O$, $^{29}Si/^{30}Si$ and $^{32}S/^{34}S$ for both GC sources. The derived $^{12}C/^{13}C$, $^{18}O/^{17}O$ and $^{29}Si/^{30}Si$ ratios averaged over both GC sources agree within uncertainties with the canonical values for the GC. Our results suggest that isotopic fractionation and/or selective photodissociation do not play any role in the determination of isotopic ratios from molecular column densities.

(v) The comparison of the excitation conditions derived for both LOSs in the centre of our Galaxy and those found for the starburst galaxies NGC 253 and M82 shows that the molecular gas in the nuclei of these galaxies have similar physical conditions.

(vi) CH_3OH is the molecule with the highest abundance difference between both GC LOSs and starburst galaxies, by factors of $\sim (1$–$6) \times 10^2$. The large difference is likely due to its photodissociation by UV radiation in starbursts.

(vii) We studied HCO^+/HOC^+, HCO^+/HCO and CS/HOC^+ ratios for both GC LOSs, typical PDR regions, starburst galaxies and the active galactic nucleus NGC 1068. We find that these abundances ratios cannot be used to distinguish between the effects of X-ray and UV radiation on the molecular clouds.

(viii) We also propose that the CS/HOC^+, HCO^+/HCO and HCO^+/HOC^+ ratios could be used as good tracers of PDR/XDR components in the molecular clouds in the nuclei of galaxies. These ratios can be used to estimate the fraction of the molecular gas affected by UV radiation. For example, the large HCO^+/HCO ratio found for LOS+0.693 indicates a PDR component of ~ 12 per cent of the total column density.

ACKNOWLEDGEMENTS

REFERENCES

Aladro R., Martín-Pintado J., Martín S., Mauersberger R., Bayet E., 2011a, A&A, 525, A89
Aladro R., Martín S., Martín-Pintado J., Mauersberger R., Henkel C., Ocaña-Flaquer B., Amo-Baladrón M. A., 2011b, A&A, 535, A84
Aladro R. et al., 2013, A&A, 549, A39
Amo-Baladrón M. A., Martín-Pintado J., Martín S., 2011, A&A, 526, A54
Apponi A. J., Pesch T. C., Ziurys L. M., 1999, ApJ, 519, L89
Bally J., Stark A. A., Wilson R. W., 1987, ApJS, 65, 13
Batrla W., Menten K. M., 1988, ApJ, 329, L117
Belloche A., Müller H. S. P., Menten K. M., Schilke P., Comito C., 2013, A&A, 559, A47
Carral P., Hollenbach D. J., Lord S. D., Colgan S. W. J., Haas M. R., Rubin R. H., Erickson E. F., 1994, ApJ, 423, 223
Churchwell E., Walmsley C. M., Wood D. O. S., 1992, A&A, 253, 541

Coil A. L., Ho P. T. P., 2000, ApJ, 533, 245
De Pree C. G., Gaume R. A., Goss W. M., Claussen M. J., 1996, ApJ, 464, 788
De Pree C. G., Goss W. M., Gaume R. A., 1998, ApJ, 500, 847
Ferrière K., 2012, A&A, 540, A50
Frerking M. A., Langer W. D., Wilson R. W., 1982, ApJ, 262, 590
Friedel D. N., Snyder L. E., Turner B. E., Remijan A., 2004, ApJ, 600, 234
Fuente A., Martín-Pintado J., Cernicharo J., Bachiller R., 1993, A&A, 276, 473
Fuente A., Rodríguez-Franco A., García-Burillo S., Martín-Pintado J., Black J. H., 2003, A&A, 406, 899
Fuente A., García-Burillo S., Gerin M., Rizzo J. R., Usero A., Teyssier D., Roueff E., Le Bourlot J., 2006, ApJ, 641, L105
García-Burillo S., Martín-Pintado J., Fuente A., Usero A., Neri R., 2002, ApJ, 575, L55
Gerin M., Goicoechea J. R., Pety J., Hily-Blant P., 2009, A&A, 494, 977
Goicoechea J. R., Rodríguez-Fernández N. J., Cernicharo J., 2004, ApJ, 600, 214
Goicoechea J. R., Pety J., Gerin M., Hily-Blant P., Le Bourlot J., 2009, A&A, 489, 771
Gordon M. A., Berkermann U., Mezger P. G., Zylka R., Haslam C. G. T., Kreysa E., Sievers A., Lemke R., 1993, A&A, 280, 208
Goss W. M., Schwarz U. J., van Gorkom J. H., Ekers R. D., 1985, MNRAS, 215, 69
Güsten R., Walmsley C. M., Ungerechts H., Churchwell E., 1985, A&A, 142, 381
Hasegawa T., Sato F., Whiteoak J. B., Miyawaki R., 1994, ApJ, 429, L77
Herrnstein R. M., Ho P. T. P., 2002, ApJ, 579, L83
Hüttemeister S., Wilson T. L., Bania T. M., Martín-Pintado J., 1993, A&A, 280, 255
Israel F. P., Baas F., 2003, A&A, 404, 495
Iwasawa K., Fabian A. C., Matt G., 1997, MNRAS, 289, 443
Jansen D. J., Spaans M., Hogerheijde M. R., van Dishoeck E. F., 1995, A&A, 303, 541
Knight J. S., Freeman C. G., McEwan M. J., Smith S. C., Adams N. G., Smith D., 1986, MNRAS, 219, 89
Koyama K., Maeda Y., Sonobe T., Takeshima T., Tanaka Y., Yamauchi S., 1996, PASJ, 48, 249
Liszt H., Lucas R., Black J. H., 2004, A&A, 428, 117
Lu F. J., Wang Q. D., Lang C. C., 2003, AJ, 126, 319
Martín-Pintado J., de Vicente P., Wilson T. L., Johnston K. J., 1990, A&A, 236, 193
Martín-Pintado J., de Vicente P., Fuente A., Planesas P., 1997, ApJ, 482, L45
Martín-Pintado J., de Vicente P., Rodríguez-Fernández N. J., Fuente A., Planesas P., 2000, A&A, 356, L5
Martín-Pintado J., Rizzo J. R., de Vicente P., Rodríguez-Fernández N. J., Fuente A., 2001, ApJ, 548, L65
Martín S., Martín-Pintado J., Mauersberger R., 2006a, A&A, 450, L13
Martín S., Mauersberger R., Martín-Pintado J., Henkel C., García-Burillo S., 2006b, ApJS, 164, 450
Martín S., Requena-Torres M. A., Martín-Pintado J., Mauersberger R., 2008, ApJ, 678, 245
Martín S., Martín-Pintado J., Mauersberger R., 2009a, ApJ, 694, 610
Martín S., Martín-Pintado J., Viti S., 2009b, ApJ, 706, 1323
Martín S., Aladro R., Martín-Pintado J., Mauersberger R., 2010, A&A, 522, A62
Mehringer D. M., Palmer P., Goss W. M., 1995, ApJS, 97, 497
Meier D. S., Turner J. L., 2005, ApJ, 618, 259
Meier D. S., Turner J. L., 2012, ApJ, 755, 104
Meijerink R., Spaans M., Israel F. P., 2007, A&A, 461, 793
Mezger P. G. Henderson A. P., 1967, ApJ, 147, 471
Mills E., Morris M. R., Lang C. C., Dong H., Wang Q. D., Cotera A., Stolovy S. R., 2011, ApJ, 735, 84
Morris M., Serabyn E., 1996, ARA&A, 34, 645
Mul P. M., McGowan J. W., 1980, ApJ, 237, 749
Müller H. S. P., Thorwirth S., Roth D. A., Winnewisser G., 2001, A&A, 370, L49

Müller H. S. P., Schlöder F., Stutzki J., Winnewisser G., 2005, J. Molecular Spectrosc. Structure, 742, 215

Nummelin A., Bergman P., Hjalmarson Å., Friberg P., Irvine W. M., Millar T. J., Ohishi M., Saito S., 1998, ApJS, 117, 427

Nummelin A., Bergman P., Hjalmarson Å., Friberg P., Irvine W. M., Millar T. J., Ohishi M., Saito S., 2000, ApJS, 128, 213

Pickett H. M., Poynter R. L., Cohen E. A., Delitsky M. L., Pearson J. C., Müller H. S. P., 1998, J. Quant. Spectrosc. Radiative Transfer, 60, 883

Ponti G., Terrier R., Goldwurm A., Belanger G., Trap G., 2010, ApJ, 714, 732

Requena-Torres M. A., Martín-Pintado J., Rodríguez-Franco A., Martín S., Rodríguez-Fernández N. J., de Vicente P., 2006, A&A, 455, 971

Requena-Torres M. A., Martín-Pintado J., Martín S., Morris M. R., 2008, ApJ, 672, 352

Rodríguez-Fernández N. J., Martín-Pintado J., Fuente A., de Vicente P., Wilson T. L., Hüttemeister S., 2001, A&A, 365, 174

Rodríguez-Fernández N. J., Martín-Pintado J., Fuente A., Wilson T. L., 2004, A&A, 427, 217

Riquelme D., Amo-Baladrón M. A., Martín-Pintado J., Mauersberger R., Martín S., Bronfman L., 2010, A&A, 523, A51

Savage C., Ziurys L. M., 2004, ApJ, 616, 966

Schilke P., Pineau des Forêts G., Walmsley C. M., Martín-Pintado J., 2001, A&A, 372, 291

Spaans M., Meijerink R., 2007, ApJ, 664, L23

Sutton E. C., Jaminet P. A., Danchi W. C., Blake G. A., 1991, ApJS, 77, 255

Terrier R. et al., 2010, ApJ, 719, 143

Turner B. E., 1991, ApJS, 76, 617

Usero A., García-Burillo S., Fuente A., Martín-Pintado J., Rodríguez-Fernández N. J., 2004, A&A, 419, 897

van der Tak F. F. S., Black J. H., Schöier F. L., Jansen D. J., van Dishoeck E. F., 2007, A&A, 468, 627

Wilson T. L., Matteucci F., 1992, Astron. Astrophys. Rev., 4, 1

Wilson T. L., Rood R. T., 1994, ARA&A, 32, 191 (W&R94)

Yusef-Zadeh F., Morris M., 1987, ApJ, 320, 545

Yusef-Zadeh F., Hewitt J. W., Cotton W., 2004, ApJS, 155, 421

Yusef-Zadeh F., Wardle M., Muno M., Law C., Pound M., 2005, Advances Space Res., 35, 1074

Zuckerman B., Turner B. E., Johnson D. R., Palmer P., Morris M., 1972, ApJ, 177, 601

SUPPORTING INFORMATION

Additional Supporting Information may be found in the online version of this article:

Table 1. Line parameters for the *LOS*+0.693.

Table 2. Line parameters for the *LOS*−0.11 (http://mnras.oxfordjournals.org/lookup/suppl/doi:10.1093/mnras/stu2271/-/DC1).

Please note: Oxford University Press are not responsible for the content or functionality of any supporting materials supplied by the authors. Any queries (other than missing material) should be directed to the corresponding author for the article.

This paper has been typeset from a TeX/LaTeX file prepared by the author.